Single-layer graphene modulates neuronal communication and augments membrane ion currents

Niccolò Paolo Pampaloni[1a], Martin Lottner[2a], Michele Giugliano[3,4,5], Alessia Matruglio[6b], Francesco D'Amico[7], Maurizio Prato[8,9,10], Josè Antonio Garrido[11,12*], Laura Ballerini[1*], Denis Scaini[1,7*]

[1] International School for Advanced Studies (SISSA), Trieste, Italy
[2] Walter Schottky Institut and Physik-Department, Technische Universität München, Am Coulombwall, Garching, Germany
[3] Theoretical Neurobiology & Neuroengineering Laboratory, Department of Biomedical Sciences, Universiteit Antwerpen, Antwerpen, Belgium
[4] Department of Computer Science, University of Sheffield, S1 4DP Sheffield, UK;
[5] Lab of Neural Microcircuitry, Brain Mind Institute, EPFL, CH-1015 Lausanne, Switzerland
[6] CNR-IOM - Istituto Officina dei Materiali, Area Science Park – Basovizza, S.S. 14 km 163,5 Trieste - Italy
[7] Elettra Sincrotrone Trieste S.C.p.A., S.S. 14 Km 163.5 in Area Science Park, I-34149 Trieste, Italy
[8]Department of Chemical and Pharmaceutical Sciences, University of Trieste, Trieste, Italy
[9]Nanobiotechnology Laboratory, CIC biomaGUNE, -San Sebastiàn, Spain
[10]Ikerbasque, Basque Foundation for Science, Bilbao, Spain
[11]Catalan Institute of Nanoscience and Nanotechnology (ICN2), CSIC and The Barcelona Institute of Science and Technology, Campus UAB, Bellaterra, 08193 Barcelona, Spain
[12]ICREA, Pg. Lluís Companys 23, 08010 Barcelona, Spain

[a] these authors equally contributed to the work
[b] Present address: CERIC-ERIC (Central European Research Infrastructure Consortium), Area Science Park, Basovizza, S.S. 14 km 163,5 Trieste, Italy

Abstract

The use of graphene-based materials to engineer sophisticated bio-sensing interfaces adaptable to the central nervous system, requires a detailed comprehension of the behavior of such materials in a biological context. Graphene peculiar properties may cause various cellular changes, but the underlying mechanisms remain unclear. Here, we show that single-layer graphene increases neuronal firing *via* altering membrane-associated functions in cultured cells. Graphene tunes the extracellular ions distribution at the interface with neurons, a key regulator of neuronal excitability. The resulting membrane biophysical changes include stronger potassium ion currents, with a significant shift in the fraction of neuronal firing phenotypes from *adapting* to *tonically firing*. By experimental and theoretical approaches we hypothesize that crucial to these effects are the graphene-ion interactions that are maximized when single layer graphene is deposited on electrically insulating substrates.

Graphene is a highly versatile two-dimensional nanomaterial widely adopted in many domains of science and technology, including advanced biomedical applications, due to its important electrical, optical and mechanical properties [1,2,3]. Graphene high carrier mobility and excellent optical transparency enabled, for example, the design of transparent electrodes in novel optoelectronic devices [4]. The combination of these features and, in particular, its remarkable electro-conductivity, makes graphene extremely appealing in neuroengineering, with reference to invasive implant technologies for brain biosensors and electrodes [5,6,7]. Despite the great interest and hopes raised by late development in graphene applications, the

understanding of the functional interactions between graphene and brain tissue is still limited, particularly concerning the close proximity of a single plain layer of carbon atoms and the nervous cells' membrane ion fluxes in a biological milieu. So far, reports have shown that graphene-based materials can be safely interfaced with active neuronal cells [8,9,10], however an in-depth study focused on the influence of single-layer graphene (SLG) on the biophysics of neurons and *ex vivo* neuronal microcircuits upon is missing. In numerous electroceuticals applications [11,12], graphene is in contact with the extracellular environment that surrounds the excitable cell membranes. We thus asked: can SLG directly or indirectly alter neuronal activity? Which manipulations of graphene might be adopted to regulate *ad hoc* these interactions? The answers to these questions appear pivotal in designing future research in bio-hybrid electronic devices and, more in general, will provide important insights on the deep interactions of technology with nature. Here, SLG obtained by chemical vapor deposition (CVD) was used to interface mammalian neurons, dissociated from the rat hippocampi, as a culture substrate. We employed different architectures of a single atomic layer graphene: (i) suspended or (ii) in contact with electrically insulating or conductive substrates. By these arrangements, we studied the collective electrical activity of neuronal networks coupled on graphene and demonstrated that, when isolated, SLG increased neuronal excitability via inducing specific changes in membrane biophysics. These consist in a significant shift of the fraction of neuronal firing phenotypes in the network from *adapting* to *tonically* firing. We then propose that graphene selectively modifies membrane-associated neuronal functions and we hypothesize a specific interaction between graphene and cations, in particular potassium, in the extracellular solution crucially regulating cell excitability.

Single and multi-layer graphene and gold substrates

Glass supported films of SLG and multi-layer graphene (MLG) were tested as substrates interfacing neuronal growth. SLG and MLG were characterized by atomic force microscopy (AFM) and compared to glass pristine (Control) and gold (Au) metalized glass samples (Fig. 1a). AFM topographies documented a surface roughness of the materials that varied from 0.23 ± 0.02 nm in Control, 1.5 ± 0.5 nm in SLG, 20 ± 10 nm for MLG and 0.47 ± 0.1 nm for Au. These values describe the surface topography, and indicate that the variations introduced by large SLG and MLG synthesis [13] results in variable patterns of low roughness, depending on the preparation method. The quality of CVD grown SLG and MLG samples was assessed by Raman and X-Ray photo-electron analysis. The recorded Raman spectra (Fig. 1b) supported the high quality of the SLG and MLG by showing low I_D/I_G ratios, indicating a low amount of sp^3 hybridized carbon atoms at grain boundaries or binding surface moieties [14]. The full width at half maximum (FWHM) of the 2D peak, as well as the I_{2D}/I_G ratio are indicative of a low bilayer content in the case of SLG [15] and turbostratic graphite in the case of MLG [16] (Fig. 1b). A graphitic Raman signature is to be expected as the MLG samples have a typical thickness of a few hundreds of layers (data not shown). The higher noise in the SLG Raman spectrum is typical for the lower Raman back scattering intensity of SLG in comparison with MLG. X-Ray photo-electron spectroscopy (XPS) analysis of SLG and MLG on Si_3N_4 reveals that both SLG and MLG samples contain a low degree of process related metal contamination (Fig. 1c).

SLG potentiates cell signaling in neuronal networks

Large films of SLG, MLG and Au were fabricated and transferred onto bare glass coverslips. To probe the electrical behavior of excitable biological cells, we used hippocampal neurons, which were dissociated from the rat hippocampi and plated directly on graphene- and Au-coated coverslips. As in our previous work with different carbon-based nanomaterial (e.g. carbon nanotubes, CNTs) [17,18,19], we did not pre-treat the culture substrates with any additional adhesion molecules, which might mask the effects of graphene. Recently, several reports described the successful growth of different cell types on graphene and graphene-based materials [9,20,21], but the *ex vivo* development and functional analysis of primary mammalian cells and neuronal microcircuits on uncoated monolayer of graphene, is rarely investigated. Neurons plated on glass coverslips were instead used as Control cultures [17,18,19]. The interface between neurons and SLG, MLG and Au, could be then directly examined, and it was found to allow the growth of cells whose mature morphology was comparable to Control ones (Fig. 2a). We further probed neuronal networks viability by quantifying network size and the ratio between neuronal and glial cells after 8-10 *days in vitro* (DIV), using immunofluorescence markers for neurons (class III β-tubulin) and astrocytes (GFAP; Fig. 2b). The histograms in Fig. 2b (right) show the surface density of cells (top) and the neuron/glia ratio (bottom) across all four conditions, which did not significantly differ (culture series used in all conditions n = 3, see Methods). In Fig. 2b, low magnification micrographs of class III β-tubulin-positive neurons also show the even distribution of cells on all growth substrates. In addition, SLG or MLG topography did not influence neuronal fibers' orientation in respect to Control or Au (see Methods). These observations, combined to the similarity of membrane passive electrical properties (see Methods) measured by single-cell intracellular electrophysiology, indicated the homogeneous growth of

healthy neurons [18] across substrates, with comparable levels of cellular composition and maturation.

When cultured, neurons develop *ex vivo* functional synaptic connections and organize their collective electrical activity as a result of recurrently interconnected networks. To assess the possible changes caused by SLG, MLG or Au on neuronal network functions, we focused on synaptic signaling and recorded spontaneous synaptic activity after 8-10 DIV. This is indirectly informative of the combined effect of existence, number, transfer gain of neuronal connections, and intensity of collective interactions between neurons. Heterogeneous post-synaptic currents (PSC) were indeed detected intracellularly as inward currents of variable amplitudes [17] in all conditions, as shown by the sample traces in Figure 2c. While the amplitude of PSCs recorded from neurons growing on SLG (n = 45), MLG (n = 20) and Au (n = 20) were similar to control conditions (n = 40) (top histogram in Fig. 2c), the PSCs frequency (bottom histogram) was significantly higher in SLG than in other conditions (i.e., Control 1.53 ± 0.22 Hz; SLG 3.21 ± 0.41 Hz; p=0.0010). Instead, both MLG, (chemically similar to SLG), and Au, (chemically different but characterized by high electrical conductivity), did not affect the frequency of synaptic events. This suggests the mechanistic involvement of specific properties of the plain sheet of carbon atoms, in the modulation of neuronal PSCs frequency, but only when assembled as a monolayer.

SLG and MLG samples were prepared by film transfer, either through polystyrene (PS) or polymethyl methacrylate (PMMA) supporting polymer (see Methods). PSCs measured in neurons showed however similar behavior when carbon based films were transferred through PMMA or PS (Supplementary Fig. 1a).

This indicates that the observed effect on PSCs is independent of the carbon film transfer method.

Under our recording conditions (see Methods), spontaneous PSCs were composed of mixed events: inhibitory ($GABA_A$-receptor mediated) and excitatory (AMPA-glutamate receptor mediated), all recorded as inward synaptic currents. These currents are characterized by different kinetics [19, 22] and were analyzed offline to gain insights into the SLG regulation of synaptic activity. In particular, the decay time constant (τ) of those currents was quantified in a subset of Control (n = 4) and SLG (n = 4) neurons. We identified slow decaying PSCs (τ = 22.4 ± 1 ms in Control; τ = 21.2 ± 1.2 ms in SLG) attributed to $GABA_A$ receptor-mediated events, and fast decaying PSCs (τ = 3.2 ± 0.2 ms in Control; τ = 3.4 ± 0.3 ms in SLG; Supplementary Fig. 1b) attributed to AMPA-receptor mediated events 22]. Fast and slow PSCs were comparably up-regulated in their frequency by SLG (Plot in Supplementary Fig. 1b).

SLG changes intrinsic neuronal firing pattern

Miniature synaptic currents (mPSCs; Fig. 3a) were then recorded in a subset of Control (n = 11) and SLG (n = 11) neurons by further application of the fast-inactivating voltage-gated sodium channel blocker, tetrodotoxin (TTX, 1 μM). As this treatment impairs the generation of action potentials (APs) and thus blocks overall network activity, recording mPSCs allows disambiguating dynamical from structural components of the emerging network activity. In particular, mPSCs reflect the stochastic release of vesicles from the presynaptic terminals at individual synapses impinging onto the recorded neuron: their frequency depends on the pre-synaptic release probability and on the number of synaptic contacts, while their amplitude depends on postsynaptic receptor sensitivity [23]. As pointed out by the box plots in

Figure 3a, we found significant difference neither in the frequency nor the amplitude of mPSCs, when recorded in Control or SLG conditions. This suggests that the increased PSCs activity described earlier in SLG does not involve structural changes in the number or in the properties of synaptic connections. This is further supported by immune-labeling experiments performed on neurons grown in Control and SLG conditions. Figure 3b shows that the number of VGlut1-positive *puncta*, used to label and identify glutamatergic presynaptic terminals [22], was not altered by the presence of SLG.

To rule out that SLG could interfere with the network composition or the maturation of inhibitory neurons, we carefully considered these two alternative hypotheses. In the first one, the fraction of excitatory to inhibitory neurons is altered by SLG (e.g. in favor of the former), thus biasing the spontaneous network electrical activity detected as PSCs. We thus performed co-immunostaining with antibodies anti-class III β-tubulin and anti-GABA (Fig. 3c) and quantified the percentage of double-positive cells in Control and SLG under confocal microscopy: a double-positive cell indicates exclusively an inhibitory neuron. In Control and SLG, we detected a comparable probability (33 ± 2.7 % in Control and 30 ± 2.5 % in SLG; n= 20 fields each) of finding β-tubulin-positive cells also positive for GABA (P = 0.21; plot in Fig. 3c), thus ruling out SLG-induced alterations in the excitatory/inhibitory balance.

In the second alternative hypothesis, SLG slows down the maturation of chloride ion fluxes through $GABA_A$ receptors. In neurons, the intracellular chloride concentration determines the amplitude of the inhibitory currents and, across successive developmental stages, shifts from higher to lower values, compared to the extracellular milieu [for recent review see 24]. Correspondingly, the activation of $GABA_A$ receptors results in a depolarizing (hyperpolarizing) drive of immature

(mature) neurons [25]. To rule out that SLG could interfere with the maturation of the $GABA_A$-mediated current drive, we performed chloride imaging in living cells, using a quinoline-based Cl^- indicator dye: MQAE (N-[6-methoxyquinolyl] acetoethyl ester) [26]. As reported in Supplementary Fig. 2a, MQAE provides high-quality labeling of neuronal cells and their processes, in both Control and SLG (left panels). When long pulses (500 ms) of pressure applications of GABA (10 mM) are delivered, efflux or influx of Cl^- are induced in the neurons, depending on their maturation, resulting in opposite changes in the Cl^--sensitive MQAE fluorescence (Supplementary Fig. 2a, middle tracings). Such changes were not detected when extracellular saline solution was pressure applied *via* the same pulses (Supplementary Fig. 2a, middle tracings). In all imaged fields (n = 20), cells displaying opposite directions of GABA-evoked Cl^- fluxes were detected, thus indicating that immature and mature neuronal phenotypes coexist within the same network. However, when these responses were quantified (plots in Supplementary Fig. 2a, right panels) no difference in their distributions was observed in Control and SLG cultures. This suggests no impact of SLG in the GABAergic system maturation *in vitro*. This was further supported by the additional quantification of the expression of NKCC1, the most abundant co-transporter membrane protein determining intracellular chloride levels, [24]: Control and SLG class III β-tubulin -positive neurons showed comparable NKCC1 expression (quantified in Supplementary Fig. 2b histograms; P= 0.37).

Thus, the SLG-mediated increase in neuronal signaling does not involve major network synaptic rearrangements, such as an increased synaptogenesis or a (de)potentiation of synaptic efficacy, nor alterations in network composition or maturation of network inhibition.

To ultimately clarify the biophysical mechanisms leading to the boost in activity exhibited only by SLG neuronal circuits, we examined directly single cell excitability by current-clamp intracellular recordings. Control and SLG neurons displayed similar resting membrane potentials (–52 ± 10 mV in SLG; –50 ± 7 mV in Control). When both classes of neurons were hold at –60 mV upon intracellular injection of hyperpolarizing current, an unbiased comparison of the basal AP frequency (Fig. 4a) could be obtained, recording in standard extracellular solution Control (n = 19) and SLG (n = 21) neurons. Consistent with the PSC observations, we detected a significantly higher AP frequency in SLG neurons than in Control ones (2.60 ± 0.36 Hz in SLG; 1.37 ± 0.26 Hz in control; P = 0.0054).

The subsequent bath addition of antagonists, selective for excitatory and inhibitory synaptic receptors, such as gabazine (5 μM), CNQX (20 μM) and APV (50 μM), was employed to functionally decouple the recorded neurons from the synaptic network. Under these conditions, intrinsic neuronal active membrane properties were evaluated evoking AP responses by stimulating cells by positive current pulses (see Methods) from the same resting membrane potential (–60 mV), [27,28]. When comparing the AP overshoot amplitude, half-amplitude AP width, threshold and AP maximal rising slope [28,29,30] in Control and SLG conditions no significant difference was found in the two groups (amplitude: 56.4 ± 3.5 mV for Controls and 59 ± 3.1 mV in SLG, P = 0.57; width: 3.5 ± 0.25 ms for Controls and 3.7 ± 0.38 ms for SLG, P = 0.59; threshold: -34.2 ± 1.5 mV Control and –35.5 ± 1.2 mV in SLG, P=0.34; maximal rise slope: 61.6 ± 7.5 mV/ms Control and 57.3 ± 5.8 mV/ms in SLG, P= 0.32). All these considerations taken together suggest no major involvement of voltage-gated fast-inactivating Na^+ channel [30, 31, 32] in explaining the observed SLG-induced effects.

In addition, at – 60 mV resting potential, under the cocktail of synaptic blockers, brief and sufficiently strong depolarizing current pulses (2-4 ms; 1 nA) easily evoked single APs in SLG (n = 25) and Control (n = 20). However, the membrane voltage trajectory of evoked single APs was followed by a transient after-hyperpolarizing (AHP) in SLG neurons while only by a small after depolarization (ADP) in control (Fig. 4b). When quantified in terms of the area below such trajectories referred to the resting potential as baseline (see the histogram in Fig. 4b), the AHP in SLG neurons was significantly different than the ADP detected in control neurons (–86.96 ± 23.60 pA·ms in SLG; +107.12 ± 21.85 pA·ms in control; P = 0.0010). Interestingly, the AHP was reduced (by 88%) by bath applying Ba^{++} ($BaCl_2$, 2 mM; n = 3), which is known to block K_{ir} and K_{Ca} membrane channels [33, 34, 35, 36]. The AHP was also reduced (by 58%) by bath applying tetra-ethylammonium (TEA, 1 mM; n = 9) a non-selective blocker of the large majority of voltage gated K^+ membrane channels (Kv) [37], including BK_{Ca} channels [38]. Finally, Apamin (200 μM; n = 5), a specific inhibitor of SK_{Ca} membrane channels [39], also strongly affected (47% reduction) the AHP (Fig. 4b, K^+ channel blockade). All these observations demonstrate that the AHP detected in SLG neurons was likely mediated by mixed K^+ conductances, including those activated by intracellular accumulation of free Ca^{++} ions [37,40]. The expression of these membrane ion channels is functionally related to the phenomenon of spike-frequency adaptation, where sustained APs discharge is progressively reduced in time. We then further examined the sustained discharge patterns of Control (n = 13) and SLG (n = 15) neurons, by injecting longer (1 s; 200 pA) depolarizing current pulses (Fig. 4c). In the majority (81.8%) of Control neurons, sustained AP firing was dominated by spike frequency adaptation, which we named *adapting* discharge phenotype and which

often even resulted in an early burst of closely spaced APs followed by a progressive decay of the spike amplitudes, leading to adaptation. On the contrary, SLG neurons (83.3%) showed no APs adaptation, which we named *tonic* discharge phenotype, where cells continuously and more regularly fired APs without apparent accommodation [41, 42]. To compare the AHP in SLG neurons upon firing of a single AP (Fig. 4b) and that elicited by multiple APs when 1 s long-stimulation was delivered (Fig. 4c), we quantified the AHP area in both conditions (Fig. 4e; –352 ± 70 pA·ms upon long depolarizing steps). Taken together, all these data hint at a complex homeostasis in the potassium membrane currents expressed by neurons when coupled to SLG substrates. This hypothesis was reinforced by results obtained under voltage-clamp from control (n = 13) and SLG (n = 15) neurons, where depolarizing voltage pulses starting from a – 60 mV holding potential baseline evoked an outward current (Fig. 4d), presumably due to the activation of a mixed population of K^+ channels. When examined under these conditions, SLG neurons were characterized by a significantly larger outward current at positive potentials, shown in the steady-state current/voltage (I/V) plot of Figure 4d, likely consequence of an up-regulation of mixed K^+ currents. All these pieces of evidence taken together strongly indicate that SLG substrates induce active changes in the electrical properties of growing neurons, presumably related to altered homeostasis of K^+ membrane currents and leading to a modulation of the single-cell firing phenotypes and ultimately to an increased network activity. Importantly, SLG neurons generated more APs when compared to Controls, even in response to milder and shorter stimuli (Supplementary Fig. 3 a and b).

Modeling the impact of firing phenotypes on network activity

The observed correlations between single-cell properties, resulting phenotype, and network effects were further investigated by mathematical modeling and computer simulations. We specifically addressed the causality between neuronal firing patterns and network activity, and we studied an established spike-rate mathematical model of the electrical activity emerging in populations of cultured neurons with recurrent synaptic connections (Fig. 5a). This model [43, 44, 45] reproduces *in silico* the spontaneous periodic occurrence of “bursts” of APs (Fig. 5b and 5c), synchronized across the network [45]. These spontaneous events are the network-level correlates of the PSCs, as well as of the spontaneous AP firing, observed in single-cell experiments. In the model, the ignition of each episode of spontaneous firing is a direct consequence of recurrent glutamatergic synaptic transmission (i.e. acting as a positive feedback) and of random spontaneous release events at synaptic terminals (i.e. as in mPSCs). The termination of each spontaneous firing episode is instead determined in the model by the combined effect (i.e. acting as a negative feedback) of inhibitory synaptic connections, transient synaptic pool exhaustion underlying communication between neurons, and spike-frequency adaptation in excitatory neurons. The last mechanism does in fact slow down the repetitive (spontaneous) firing and thus decrease the synaptic net currents to downstream neurons.

We simulated a network of 1600 model neurons with a fraction of excitatory to inhibitory neurons equal to 80/20, reminiscent of the neuronal composition *in vitro* (Fig. 3c) [46]. As most of inhibitory neurons are known from the literature to display only a tonic electrical phenotype, we hypothesized that the change in the ratio between adapting and tonically firing neurons observed in our experiments, occurred in excitatory neurons only. We therefore included in the model two subpopulations of

excitatory neurons: one displaying *adapting* phenotype and one displaying *tonic* phenotype. We then found that the higher the relative fraction of *tonic* firing neurons, the higher the rate of occurrence of synchronized bursts (Fig. 5b and 5c). This supports the conclusion that the experimentally observed increase in the frequency of spontaneous (PSCs/APs) activity (Fig. 2c, SLG) is caused by the different ratio of cells with adapting/non-adapting neuronal electrical phenotypes.

The potassium ions hypothesis

By a more biophysically-detailed modeling approach, we then asked at the single-neuron level whether an increase in the total outward ionic conductance or, alternatively, a small reduction in the extracellular concentration of K^+ ions were responsible for the observed changes in single-cell firing activity. To that aim we studied *in silico* the effects on excitability of (i) an increased total outward potassium conductance or of (ii) a modest depletion of extracellular potassium. The rationale behind these computer simulations is that either SLG induced a chronic increase in ion current involved in firing activity regulation, or SLG acutely altered cell firing by changing ion mobility. The two hypotheses are not mutually exclusive.

As a proof of concept, we considered the simplest possible model of AP generation, as proposed by Hodgkin and Huxley (HH) [47]. This model describes the generation of a (train of) AP(s) in terms of the known interplay between *fast-inactivating* (~1 ms) inward Na^+ currents and *delayed rectifier* outward K^+ potassium currents (Fig. 5d). Of course, by no means these are the only membrane currents underlying the electrophysiological behavior of rat hippocampal neurons [48]. Nonetheless, by stripping down excitability to its bare essential we could explore whether stronger outward potassium currents may favor excitability and not always oppose to it, as

intuitively expected. We found that the progressive sodium current inactivation (Fig. 5d, lower left, green traces) – occurring in the HH model only over *fast* and not slow time scales – could be counterbalanced and reversed by strong K^+ currents (Fig. 5d, lower right, red traces). This results in a sustained, tonic, response to an external current stimulus (i.e. compare Fig. 5d to Fig. 4c), instead of a progressive inactivation of the firing. While this effect is reversed by simulating an overexpression of Na^+ channels (e.g. at the axon initial segment – not shown), it serves us here only as a proof of concept of a counter-intuitive phenomenon: increasing outward currents increases cellular excitability (i.e. by removing sodium current inactivation). Of course, an *ad hoc* increase in the maximal conductance of sodium ion channels also increases excitability, although – in the mathematical model – with distinct features in the type of transition associated to the *limit cycle* to sustained AP firing (Supplementary Fig. 4). The role of sodium inactivation has been investigated in previous experiments in the cortex and spinal cord [49,50] and proposed to contribute to spike adaptation. While we cannot rule out a role for impaired Na^+ inactivation in SLG neurons, we believe that the strongly enhanced AHP prevents the membrane potential to reach levels at which inactivation is fully expressed to limit firing.

Figure 5e further illustrates this phenomenon, across distinct stimulus current amplitudes and over three levels of K^+ conductances. Therefore, in the model the more K^+ channels (i.e. same type or distinct type) the higher the excitability, in those regimes where progressive sodium inactivation affects neuronal firing.

However, as outward K^+ currents also depend on the ionic driving force beyond on the maximal conductance (i.e. in our model, $I_K \sim G_K\ (E_K - V)$ - see Methods), theoretically a change in the local ionic composition might reverse sodium

inactivation too. In fact, the Nernst equilibrium potential E_K is determined by the K^+ concentration gradients outside and inside the neuronal membranes and it assumes negative values under physiological condition [51]. Should SLG interfere extracellularly with K^+ bulk diffusion in its proximity (see below) then a depletion of K^+ (e.g. 10-20%, as $[K^+]_{EX} \rightarrow \delta \cdot [K^+]_{EX}$, $\delta = 0.8 - 0.9$), would lead to an increase in the ionic driving force, because E_K would then decrease accordingly (i.e. ~2-5 mV). By definition

$$E_K = \frac{RT}{zF} \cdot ln\left(\frac{\delta \cdot [K^+]_{EX}}{[K^+]_{IN}}\right) = E_{K\ control} + \Delta$$

where T is the absolute temperature, R the universal gas constant, F the Faraday constant, and z = 1 K^+ valence (i.e. $RT/zF \sim 25\ mV$ at room temperature), and $\Delta = RT/zF \cdot ln(\delta)$ is a negative quantity measured in mV. By numerical simulations (Fig. 5f), we found that a modest decrease in E_K in the model (e.g. from –75 to –77.6 mV) could indeed counterbalance sodium inactivation, at least for an intermediate external current stimulus intensity and without altering significantly the resting membrane potential.

All in all, this last part of our modeling effort suggests a specific involvement of the extracellular concentration of K^+ in neuronal excitability: the less extracellular K^+ the higher the excitability, at least in those regimes where progressive sodium inactivation affects neuronal firing disfavoring sustained *tonic* response.

It is therefore tempting to speculate that changes in excitability of cells coupled to SLG might be caused by an extracellular reduced mobility of K^+ at the interface between the nanomaterial and the extracellular solution, leading to a K^+ depletion at the neuronal membranes. *Per se*, this would explain directly the change in neuronal

phenotype, but indirectly could account for a homeostatic re-arrangement of neuronal excitability by up-regulating number or conductance of K^+ channels.

Localized potassium ions depletion in cell-substrate cleft

We hypothesize that at the core of SLG ability to alter neuronal excitability is the ion adsorption on graphene surfaces. This may result in a modification of ion mobility, in particular K^+, at the neuronal/graphene interface.

Within this proposed mechanism, it is still unclear how SLG might actually modify K^+ ion mobility while MLG (or Au) do not. It is well known that carbon-based π electron-rich surfaces in ionic solutions show a significant surface enrichment of cations due to specific cation-π interactions [52, 53, 54, 55]. Because of its size, in solution, K^+ ions are more weakly solvated by water, when compared to other species (e.g. Li^+ or Na^+ ions), but are still good π binders. This feature makes K^+ the best alkali metal binder to carbon-based surfaces in aqueous solutions [54, 55]. This implies that, in nanoscale-confined systems, cation trapping occurring at the carbon surface level may lead to a significant local depletion of ions, in particular potassium, at the neuronal membrane surface level.

In order to address this point Raman spectroscopy (sketched in Supplementary Fig. 5a) was performed on supported SLG and MLG samples in liquid condition without and in the presence of KCl and NaCl at physiological concentrations (4 mM and 150 mM, respectively) into the solution. Graphene-related G vibrational peak [15] was evaluated in wave number position for both SLG (Fig. 6a, left) and MLG substrates (Fig. 6a, right) with samples totally immersed in pure deuterium oxide (D_2O), in D_2O solution containing 4 mM KCl, and in D_2O solution containing 150 mM NaCl (see Supplementary Methods for technical details). The wavenumber maximum position

relative to the G-peak Raman shift for control SLG sample was collocated at 1599 ± 0.5 cm^{-1}. It exhibited a change in shape associated to a G-peak position shift to 1600 ± 0.5 cm^{-1} and to 1602 ± 0.5 cm^{-1} in the presence of NaCl and KCl D_2O solutions, respectively (Fig. 6a, left, inset). Conversely, in MLG samples G peak maximum position did not change (Fig. 6a, right, inset). The mechanisms responsible for the observed shift in the G Raman band of graphene with, more importantly, the narrowing of the G band (FWHM) detected in SLG when samples are immersed in a KCl solution could result from charge doping [56] or internal strain [57]. More specifically, the shifts in G band position exhibited by SLG samples in the presence of salt solutions could be indicative of a specific cation interaction, not measurable in the case of MLG. Notably, the larger G band Raman shift in KCl treated samples (3 ± 0.5 cm^{-1}) than in the presence of NaCl (1 ± 0.5 cm^{-1}) correlates well with a larger SLG affinity for K^+ when compared to Na^+. This result, observed here for the first time, is in agreement with theoretical studies on cation-π interaction in solvated conditions [54,55]. This specific graphene–K^+ interaction taking place in aqueous phase is supported by Raman analysis of SLG substrates in dry (air) condition (see Supplementary Fig. 5b). In fact, as predicted by gas-phase simulations [54, 55], in this case a stronger graphene–Na^+ interaction (G peak shift of about 4 ± 1 cm^{-1} than control SLG) is detected than graphene–K^+, confirming the role of cations and the specificity of potassium in the aqueous environment and further sustaining theoretical studies [54, 55].

In our experimental settings, cultured neurons are characterized by a cell body displaying a “disk-like” shape with average diameters of about 10 μm (Fig. 2a and 2b and Fig. 3b). Studies of cell/electrode interfaces in culture showed typical cleft thicknesses between 40-100 nm [58,59,60], corresponding to a cell-substrate

cleft volume of about 3-8 μm^3. Similar dimensions were found in our samples by SEM images of cell cross sections at membrane-substrate interface obtained by focused ion beam (FIB; Supplementary Fig. 6). At an extracellular KCl concentration of 4 mM (see Methods), ~$7\text{-}20 \cdot 10^6$ K^+ ions would occupy such a volume in the bulk. Under these conditions, the specific cation-π interaction at surface level could result in partial K^+ depletion from the extracellular solution facing the cell membrane. Taking into account, in first approximation, a 40:1 ratio between Na^+/K^+ cations in solution, and considering the contribution of both inner and outer hydration shells [61] to evaluate a reasonable cross-section of interaction between K^+ and graphene, we can assume that at least $2 \cdot 10^6$ K^+ will be strongly adsorbed on the surface. This could be translated in a theoretical local depletion of potassium ions of about 10-20% (Fig. 6b), this value is in accordance with what examined by our single-cell neuron model (Fig. 5e and 5f). Such a depletion profile has been inferred mesoscopically by the steady-state diffusion equation with *ad hoc* boundary conditions.

Substrate modulation of graphene cation-π interaction

Our experiments have shown that SLG behaves differently from MLG in respect to the K^+ homeostasis of neurons and subsequent improved excitability. The two nanomaterials culturing platforms, SLG and MLG, differ only in the conductive properties of the supporting structure immediately below the first mono atomic carbon layer exposed to the biological milieu (i.e., on one hand glass and on the other multiple layers of graphene/graphite). MLG can be regarded, form the point of view of a neuron growing on its top, as a SLG film layered on the underlying, electrically conductive, MLG. In our hypothesis, graphene efficiency in trapping K^+

ions is tuned or influenced by the electrical properties of the supporting structure [62, 63].

In this framework, we investigated if the electrical properties of the supporting material might *per se* tune SLG ability to affect neurons. We compared PSCs in neurons directly grown on glass (Control), on free-standing SLG (Suspended SLG, see Methods) and on SLG transferred on an insulating substrate (SLG on glass) and on a conductive substrate of indium tin-oxide (SLG on ITO). The last is an optically transparent and smooth film with well-defined electrically conductive properties and topography [19]. In Figure 6c the results of such experiments are summarized and are in full accordance to our hypothesis: the PSCs frequency was boosted by SLG on glass (3.11 ± 0.35 Hz *vs.* 1.72 ± 0.21 Hz, P = 0.031) and even more by suspended SLG (4.22 ± 0.35 Hz *vs.* controls, P = 0.001), while no effects were detected when SLG was layered on ITO. Notably, in suspended SLG, PSCs amplitude is also significantly increased (59.2 ± 5.8 pA *vs.* 35.9 ± 4.9 pA, P = 0.017) when compared to control cultures.

It is not trivial to understand the exact mechanism underlying this phenomenon but, in the absence of any theoretical model describing the dependency of graphene π-cation interaction on supporting surface properties, we speculate that surface conductivity is playing a key role. In particular, in suspended SLG, environmental disturbances are minimized allowing access to the intrinsic properties of graphene close to the unperturbed Dirac point. Superficial charge inhomogeneity is reduced in this case compared to supported samples giving rise to a “close-to-theory” system [1,64] (Fig. 6d, left) that will fit better to cation-π simulations’ results [42,43,44]. SLG laying on metal surfaces usually undergo electron-doping resulting in a down-shift of graphene Dirac point [65] (Fig. 6d, middle). This will induce a homogeneous charge-

distribution [66] that could result in a reduction of graphene cation-π interaction force. On the other hand, in SLG transferred on insulating substrates as, for example, glass or SiO_2, there are significant local fluctuations in surface potential [67,68], thus inducing an inhomogeneous charge distribution on graphene surface where neutral areas, where SLG band structure is basically unperturbed as in the case of suspended graphene, and p-doped areas, coexist [69,70]. In the latter case, the interaction of graphene with potassium will be still present even if its net effect is less pronounced than on suspended SLG.

In this picture, MLG behavior can be described as that of SLG when laying on a (semi)-metallic graphite substrate [71] falling, in this case, in the second case we previously discussed [72].

Our preliminary Raman results can explain the different behavior of SLG towards K^+ or Na^+ and the difference between SLG and MLG behavior in ion solution. However, do not directly demonstrate differences between SLG and MLG in ion absorbance. In fact, the adsorption of ions on SLG, when on insulating substrates, may induce non homogeneous densities of charge carriers in the monolayer that are measured by Raman spectroscopy, while such interactions are prevented, and thus not measured by Raman, when carriers are distributed in the bulk conductive substrates (the multiple graphene layers in MLG) and not confined to the SLG layer.

We conclude that SLG modifies neuronal excitability and we propose a provocative hypothesis: that this effect is mediated by graphene ability to restrict K^+ ions mobility in close proximity to the material surface, but only when the monolayer is deposited on electrically insulating substrates. Indeed, we cannot exclude additional mechanisms related to non-uniform charge carrier densities, affecting

surface concentrations of ions [73]. Alternatively, restricted ion mobility might affect the way astrocytes regulate the extracellular *milieu* between graphene and neurons. Ultimately, we provided multiple lines of evidence to demonstrate that SLG, when engineered on an insulating glass substrate, is able to tune neuronal excitability. Our physiological experiments demonstrate that the detected increase in neuronal synaptic activity is caused by increased cell firing, rather than to changes in network size, synaptic density [74,75,76], inhibition/excitation ratio or inhibition maturation. We also demonstrated that neurons, when exposed to SLG, up-regulate outward currents, in particular potassium ones and switch to functionally-tonic firing phenotypes. Our computer simulations support the notion that changes in the ratio of adapting/firing neurons will impact the global network activity [77,78] and suggest the key contribution of up-regulated potassium currents in driving this change. All these effects are not mimicked by MLG or other conductive substrates such as Au. We propose that, due to the cation-π interactions of graphene, cations, and K^+ in particular [53,54,55], will be trapped at the graphene surface, resulting in a graded depletion of such ions at a distance from the material compatible with the nanometer scale characterizing cell adhesion mechanisms [79,80]. This hypothesis is grounded in earlier molecular dynamics simulations at the equilibrium [53], where ionic enrichment occurs at the interface. As in a random-walk with a “sticky/viscous” wall, free potassium ions at the interface would be largely depleted, while their concentration would be unaffected in the bulk, i.e. far from the graphene surface. Therefore, at the nanoscale, at a distance compatible with realistic cell membrane proximity, a vertical K^+ spatial gradient may not be compensated entirely, as it is likely to be restricted at the interface with graphene by the tortuosity of the extracellular microenvironment, densely packed with macromolecules for cell

adhesion as well as cell membranes of neighboring cells [81]. This will translate in a slight but effective reduction of free extracellular potassium in the sub-micrometrical extracellular space confined between graphene and the overlying neuronal membrane. The effectiveness of such a K^+ depletion in altering cell excitability is grounded by our mathematical single-cell biophysical model.

We cannot rule out that the up-regulation of K^+ outward currents and the switch in firing patterns could be induced by other chemical or physical features of SLG Intriguingly, in our previous studies, when interfacing neurons with CNTs (basically rolled up graphene sheets) randomly piled in dense mashes, we never observed increases in AHP, supporting the suggested mechanisms dependent on the intrinsic properties of SLG. Differently from SLG, CNTs boosted synaptogenesis and molded the integrative abilities of cultured hippocampal neurons, probably due to their shape, conductivity and roughness, mimicking extracellular matrix and promoting tight nano-contacts between neuronal membranes and CNTs supporting a direct electrical coupling between CNTs and neuronal membranes [18,19]. In more complex systems, CNTs scaffolds were reported also to increase and guide axonal re-growth and orientation [9,82].

The precise mechanisms for the observed effects of SLG substrates in this study are still elusive. We put forward a novel hypothesis based on the specific properties of the materials characterized by π electron-rich one plain layer of carbon atoms and we focused in particular on the specific cation-π interactions [48].

We further postulate that in the case of SLG, the more unperturbed its band structure is, the larger is its ability to deplete potassium ions at the interface with neuronal membrane. Naturally, we cannot exclude alternative possibilities, but our results with suspended and ITO–supported SLG are consistent with our hypothesis. Despite

these considerations on hypothetical mechanisms, the results reported here indicate that graphene properties might affect neuronal information processing *in virtue* of the physical interactions of such a nanomaterial with the biological environment. Novel and outstanding materials might then represent, in general, unconventional and exciting tools to gain insights into genuine biological processes.

METHODS

Substrate fabrication

SLG was CVD grown on ultraflat Cu surfaces and transferred, as previously described [83], onto SiO_2 and Si_3N_4 substrates for subsequent Raman and XPS characterization. Briefly, after annealing the Cu foil in a 400 sccm :100 sccm argon and hydrogen atmosphere at 100 mbar and 1015 °C, a SLG layer is nucleated at 15 mbar with 0.2 sccm methane, and closed by successively increasing the methane content to 0.5 sccm. The graphene is transferred using PMMA (PMMA 950K A2, MicroChem, USA) or PS (Polystyrene MW ~192k, Sigma-Aldrich, USA). For neuronal culturing, SLG was transferred to glass coverslips or indium tin oxide (ITO). Before the transfer procedure, hosting substrates were ultrasonicated in acetone and isopropanol to assure the required cleanness. Glass and ITO coverslips followed an additionally cleaning step in concentrated HCl overnight. MLG sheets were CVD grown on Ni ultraflat surfaces as described previously [84] and transferred on hosting substrates following the same procedure adopted for SLG. Briefly, the Ni foil was annealed as described before, at a temperature of 900 °C. After annealing, a methane flow of 10 sccm at 50 mbar enabled to the diffusion of carbon into the foil, which then, during the following slow cooling step, precipitated to a layer of MLG on the surface.

Gold samples have been prepared starting from glass rectangular slides (24 mm x 12 mm, 0.2 mm thick), cleaned previously in Piranha solution (H_2SO_4:H_2O_2, 5:5 ratio in volume) in order to remove eventually present organic contaminants. Subsequently, 15 nm of Au were thermally evaporated at a rate of 0.5 Å/s. A thin adhesion layer of 5 nm of Cr was used in order to improve Au/glass adhesion. A quartz crystal microbalance was used as thickness control.

To obtain suspended graphene structures, graphene is transferred on patterned substrates obtained using OrmoComp® (micro resist technology, GmbH), a flexible and biocompatible inorganic-organic material. The OrmoComp® substrates have been prepared on circular glasses (5 mm of diameter, 0.12 mm-thick), previously cleaned in Piranha solution (H_2SO_4:H_2O_2 5:5 % v/v) in order to remove organic contaminants. Subsequently, a poly-dimethylsiloxane (PDMS) master is prepared with replica molding process starting from a silicon stamp which is patterned with an array of parallel lines of width and periodicity of 10 μm and 20 μm, respectively. The OrmoComp® master is used to press a drop of OrmoComp® on the circular glass in order to transfer the micropattern. Finally, the OrmoComp® is cured with UV light and the PDMS master is released. Commercially available single-layer CVD graphene on copper (Cu; GRAPHENEA – San Sebastián, Spain) is wet-transferred on the OrmoComp® substrates following the protocol described by Matruglio *et al.* [85]. Briefly, a layer of 250 nm of mr-I 7020 (a thermoplastic polymer of Micro Resist technology GmbH) is used as sacrificial layer and spin coated on the graphene/Cu. The polymer/graphene/Cu membrane is placed in a copper etching solution ($FeCl_3$:H_2O 3:7 % v/v), etched overnight and finally washed in DI water in order to remove any residual due to the etching solution. The transfer of graphene is performed fishing the polymer/graphene/Cu membrane into the water directly on the

OrmoComp® substrate. The water is left to evaporate at room temperature for 2 h, and mr-I 7020 is dissolved in cold acetone for 5 minutes. Critical point drying process is performed in order to avoid the collapse of the suspended structures.

Cell culture and electrophysiology

Isolation of primary brain tissue was carried out in accordance with the recommendations in the Guide for the Care and Use of Laboratory Animals of the National Institutes of Health and the appropriate international and institutional standards for the care and use of animals in research (Italian Ministry of Health, in agreement with the EU Recommendation 2007/526/CE). The protocols in this study and all performed experiments are approved by the local veterinary service and the institutional (SISSA) ethical committee, in accordance with the EU guidelines (2010/63/UE) and Italian law (decree 26/14).

Dissociated hippocampal cultures were obtained from neonatal rats (P0–2) as previously described [17,18,19], and were plated on poly-L-Ornithine coated (SIGMA; Control), SLG-, MLG- or Au-covered glass coverslips. Cultured cells were incubated at 37 °C, 5% CO_2 in culture medium composed of Neurobasal-A (Thermo Fischer) containing B27 2% (Gibco) Glutamax 10 mM and Gentamycin 0.5 μM (Gibco), and used for experiments at 8–10 days *in vitro* (DIV).

Somatic whole-cell patch clamp recordings were performed at room temperature (20-22 °C) with pipettes (4-7 MΩ) containing: 105 mM K gluconate, 20 mM KCl, 10 mM HEPES, 4 mM MgATP, 0.3 mM GTP, pH 7.35. The external saline solution contained: 150 mM NaCl, 4 mM KCl, 1 mM $MgCl_2$, 2 mM $CaCl_2$, 10 mM HEPES, 10 mM Glucose, pH 7.4. Under voltage-clamp mode we measured the neuronal passive membrane properties: input resistance and cell capacitance did not significantly

differ between the four groups (in control 592 ± 51 MΩ, 74 ± 5 pF, n = 47; in SLG 664 ± 57 MΩ, 83 ± 4 pF, n = 54; in MLG 614 ± 74 MΩ, 85 ± 5 pF, n = 18; in Au 656 ± 65 MΩ, 80 ± 6 pF, n = 17). In voltage clamp experiments, the holding potential (V_h) was –56 mV, not corrected for liquid junction potential, that was calculated to be –14 mV in our experimental conditions; the uncompensated value for series resistance (Rs) was < 8-11 MΩ.

Single spontaneous synaptic events (PSCs) and miniature PSCs (mPSCs) were detected by the use of the AxoGraph X (Axograph Scientific) event detection program [86] and by the Clampfit 10 software (pClamp suite, Axon Instruments). On average, ≥ 400 events were analyzed from each cell in order to obtain mean frequency and amplitude parameters. Glutamate AMPA-receptor and $GABA_A$-receptor mediated PSCs were isolated offline by building two templates with different kinetic parameters: respectively 0.1 ms rise-time; 3 and 30 ms decay time constant (τ); 10 and 100 ms template length. Previous work [19,22] indicated that in our experimental conditions, the vast majority of fast-decaying (τ < 5 ms) PSCs are mediated by the glutamate AMPA-receptor type; while the slow-decaying (τ > 20 ms) PSCs are mediated by the $GABA_A$-receptor type.

Current-voltage relations (I/V plots) were obtained by applying hyperpolarizing or depolarizing voltage steps (15 steps of ΔV = 10 mV; 500 ms duration) from –110 mV to + 30 mV (values corrected for liquid junction potential) in the presence of 1 μM Tetrodotoxin (TTX; Latoxan). A least square routine was fitted to the linear part of the I/V curve, the slope of which was used to calculate leak conductance. Assuming that a leak conductance is time and voltage independent, the I/V plot were corrected for leak currents by subtracting the observed currents from the extrapolated leak

currents at the same level of test potential and the current values were then normalized to the cell capacitance [87].

In current clamp recordings, bridge balancing was continuously monitored and adjusted. Action potentials (APs) were isolated off line by setting an appropriate threshold voltage (10 mV). The fast voltage transients that crossed this value were identified as APs and the spontaneous firing frequency for each neuron was calculated on a sample of at least 5 min of continuous recording keeping (by negative current injection) at –60 mV the resting membrane potential.

At -60 mV resting membrane potential, the AP properties were experimentally determined by depolarizing (0-200 pA, in 20 pA increments) current steps (500 ms). The first AP produced by the current-clamp series was used for single AP measurements, including amplitude, threshold, duration at half-amplitude and maximal rising slope [27,28,30]. The threshold for firing was determined by measuring the voltage at the upward deflection of the trace, maximal AP amplitude was measured from threshold to the peak of the spike, the duration was measured at half-amplitude from threshold to peak and the maximal rising slope was measured as max dV/dt in the selected area of the voltage tracings (all measures performed by Clampfit; pClamp suite, 10.2 version; Axon Instruments). In evoked APs, the AHP was quantified over a window of 100 ms by calculating the area below or above the voltage curve, starting 20 ms after the beginning of the AP.

AP discharge patterns were investigated by delivering depolarizing current steps (1 s) of 200 pA while keeping the cells at –60 mV resting potential with steady intracellular current injection. “Adapting” and “tonic” responses were identified as previously described [42]. In some experiments, depolarizing current pulses ranging

from 150 to 250 pA were used to investigate the dependence of the firing pattern on the stimulus intensity, that did not change across these values.

Beside the monitoring of the spontaneous firing frequency, all the current clamp experiments were carried out in presence of the synaptic blockers (all from Sigma) CNQX (10 μM), Gabazine (5 μM) and APV (50 μM) added to the external solution. Current and voltage clamp responses were digitized at 20 kHz with the pCLAMP 10 software (Molecular Devices) and stored for further analysis.

Immunohistochemistry

Hippocampal neurons were fixed with 4% formaldehyde (prepared from fresh paraformaldehyde) in PBS for 20 min, permeabilized with 0.3% Triton-X-100 for 10 min and subsequently incubated with primary antibodies for 30 min at RT. After washing in PBS cultures were then incubated with secondary antibodies for 45 min and then mounted in *Vectashield* (Vector Laboratories) on 1 mm thick microscope glass slides. As primary antibodies were used rabbit polyclonal anti-β-tubulin III (Sigma T2200, 1:250 dilution), mouse monoclonal anti-GFAP (Sigma-Aldrich, 1:200 dilution), and guinea pig anti-vesicular glutamate transporter 1 (VGLUT1; Millipore, 1:2000). As secondary antibodies were used Alexa 594 goat anti rabbit (Invitrogen, dilution 1:500), Alexa 488 goat anti mouse (Invitrogen, dilution 1:500), and Alexa 488 goat anti guinea-pig (Invitrogen, 1:500). To stain cells nuclei, we used DAPI (Invitrogen, 1:200 dilution). To quantify cell density, images were acquired with an Epifluorescence Microscope (DM 6000, Leica; 10× objective). We collected 10 fields (1000 μm × 500 μm) per coverslip (n = 30, 3 culture series for control, MLG and Au) and analyzed fluorescence signals using ImageJ software (http://rsb.info.nih.gov/ij/).

To evaluate the orientation of the re-growing axons on the various substrates, we quantified their relative orientation based on the directionality analysis [82,88]. Briefly, the mean fiber's relative dispersion was computed from n = 5 randomly sampled images per condition (Control, SLG, MLG and Au) where neuronal processes were visualized by class III β-tubulin immunofluorescence (Fig. 2a). The analysis was carried out using the Directionality plugin of Fiji software inferring the preferred orientation of "structures" present in the input image. Fiber orientation was calculated via a Fourier component analysis [88]. We found no significant differences in the direction of the mean fiber's dispersion among different conditions (Control = 30 ± 9°; SLG = 29 ± 7°; MLG = 38 ± 8°; Au = 35 ± 9°) indicating a negligible impact of the substrate on the orientation of the neuronal processes.

To quantify VGlut1 puncta, n = 20 ± 10 z-stacks (acquired every 0.4 μm) were taken from n = 10 randomly selected fields (160 μm × 80 μm) per coverslip (n = 30, 3 culture series in Control and SLG) using an inverted confocal Microscope (Nikon Eclipse Ti-E; 40x oil immersion objective, 1.3 NA). To quantify VGlut1 puncta, we selected only VGlut1-positive puncta (< 2 μm^3) touching the β-tubulin III positive signal; for each image VGlut1 puncta were normalized to the β-tubulin III positive volume. Images were analyzed using the Volocity software (Perkin Elmer).
To highlight GABAergic neurons, cultures were stained with anti-GABA polyclonal primary antibody produced in rabbit (SIGMA, A2052: 1:500). To label the NKCC1 co-transporter, we used anti NKCC1 rabbit polyclonal primary antibody (Abcam; AB59791; 5 μg/ml). Cultures were then stained with class III β-tubulin primary antibody produced in mouse (SIGMA; T5076; 1:500). As secondary antibody, we

used AlexaFluor 488 goat anti rabbit (ThermoFisher A11034; 1:500), and AlexaFluor 594 goat anti mouse (ThermoFisher, A11032; 1:500).

To quantify the percentage of GABA-positive neurons, 10 ± 5 confocal z-stack (Nikon PlanFluor 40× / 1.3 NA) were acquired from randomly selected fields (n = 20 for Control and n = 20 for SLG) and GABA-positive neurons were counted. This value was then normalized to the overall number of neurons (class III β-tubulin - positive cells) for each field. To quantify NKCC1 puncta, n = 10 z-stacks (acquired every 0.25 μm) were taken from n = 20 randomly selected fields (106 μm × 106 μm) each group, using an inverted confocal Microscope (Nikon Eclipse Ti-E; Nikon Plan Apo Lambda 60x oil immersion objective, 1.4 NA). To quantify the amount of neuron-related NKCC1, only NKCC1-positive puncta in contact with the β-tubulin III signal were selected.

Imaging

For Cl^- imaging experiments, primary hippocampal cultures (DIV 8-10) were loaded with the fluorescent Chloride indicator MQAE (Abcam; ab145418) diluted in the standard extracellular solution at a final concentration of 1 mM for 10 min at 37 °C in the cell culture incubator. Samples were then washed in the extracellular solution for 10 min at 37 °C. Samples were placed in a recording chamber mounted on an inverted microscope (Nikon Eclipse Ti-U) and observed with a 60× objective (0.7 NA, PlanFluor, Nikon). Images (1024 × 1024 pixels) from fields containing 7 ± 4 neurons were acquired for 2 minutes (at 5 frame s^{-1}) by a Hamamatsu Orca-Flash 4.0 digital camera, exciting the MQAE dye with a 330-380 nm wavelength light generated by a mercury lamp. Excitation light was separated from the light emitted from the sample using a 400 nm dichroic mirror (Nikon UV-

2A) and ND filter (ND 16). Images of emitted fluorescence >420 nm were displayed on a color monitor controlled by an integrating imaging software package (HC Image, Hamamatsu) using a personal computer. Recorded images were analyzed offline with the Clampfit software (pClamp suite, 10.2 version; Axon Instruments). Intracellular Cl^- transients were expressed as fractional amplitude variations (ΔF/F0, where F0 is the baseline fluorescence level and ΔF is the change over baseline); the onset time of neuronal activation determined by detecting those events in the fluorescence signal that exceed at least five times the standard deviation of the noise. To elicit chloride influx/efflux through the membrane, an injection pipette (patch pipette with resistance of 1–4 MΩ, filled with 10 mM GABA diluted in the extracellular solution) was positioned at 20-50 μm from the cell soma and connected to a pico-spritzer (PDES-02DX, npi Electronics) with 0.5/1 psi in-line pressure, 500 ms. GABA puffs were delivered at fixed times. At the beginning of each experiment, a pipette containing pure saline was used to exclude artifacts due to the pressure injection (Supplemental Fig. S2). Individual images were analyzed to measure the intensity of MQAE in selected region of interest (ROI). We found an overall percentage of 37 ± 6.5 % Control neurons and 35.6 ± 9.3 % SLG neurons that did not respond to the stimulation, and were excluded from further analysis.

Electron microscopy (EM)

Scanning EM imaging was conducted using collecting secondary electrons on a Gemini SUPRA 40 SEM (Carl Zeiss NTS GmbH, Oberkochen). Before SEM imaging, neuronal cells grown on the different substrates were fixed in 3% Glutaraldehyde in 0.1 M Sodium Cacodylate Buffer (pH 7.4), then dehydrated sequentially in ethanol solutions of 50, 75, 95, 99 and 100% (vol/vol in H_2O, 3

minutes each, 4 °C). After overnight drying in the fridge, and before imaging samples were metalized with a 5 nm thick layer of platinum-iridium allowing using a metal sputter coater (Polaron SC7620). In order to prevent electron induced surface charging, low accelerating voltages (0.8-1.5 keV) were used for brain slices visualization.

SEM images of cells cross sections at membrane-substrate interface were obtained by focused ion beam (FIB) using a LEO-ZEISS Cross-Beam 1540 XB system. Gallium ion beam milling was performed with a current beam of 30 mA while SEM images were collected at 3 kV. Samples were prepared following the same procedure described in the previous paragraph.

Substrate characterization

AFM topography data (MFP-3D, Asylum Research, Santa Barbara, California, USA) was acquired in tapping mode, using silicon cantilevers in ambient conditions. The roughness estimates were calculated using the standard deviation of elevation in mapped surface areas with sizes of 10 μm x 10 μm. XPS spectra were recorded in ultra-high vacuum conditions using a monochromatic SPECS XR-50 Mg Kα X-Ray source ($E_{K\alpha}$ = 1253.6 eV) and a hemispherical energy analyzer (Phoibos 100/150, Specs, Berlin, Germany). μ-Raman spectra were recorded with an in-house built system using an Ar-ion laser at 514.5 nm and operating with a spectral resolution of 0.75 cm^{-1}.

Raman measurements in aqueous conditions have been carried out at on the IUVS beamline at Elettra synchrotron radiation facility (Trieste, Italy). A complete description of the experimental apparatus can be found elsewhere [10.1016/j.nima.2012.11.037]. A 532 nm laser source, with a beam power near 5

mW, has been employed as excitation source. The scattered radiation was collected in a backscattering geometrical configuration. Slight modifications on the standard backscattering set-up have been introduced to allow measurements in liquid conditions (see Supplementary Methods). A 750 mm focal length Czerny-Turner spectrometer, equipped with an holographic reflection grating of 1800 g/mm and coupled with a Peltier-cooled back-thinned CCD, has been used to get the final Raman spectra.

Data Analysis

All values from samples subjected to the same experimental protocols were pooled together and expressed as histograms (mean ± SEM with n = number of cells, unless otherwise indicated) or through box-plot representation when one or more data set were found to follow a non Gaussian distribution. In box-plots, the thick horizontal bar indicates the median value, the boxed area extends from the 25^{th} to 75^{th} percentiles while whiskers from the 5^{th} to the 95^{th} percentiles. The homogeneity of variances was assessed through the Levene's test.

Statistically significant difference between two data sets was assessed by Student's t test for parametric data and by Mann-Whitney for non-parametric ones. Differences between the logarithmic values of the analyzed variables were assessed using one-way ANOVA [89] and multiple comparisons were adjusted by Bonferroni correction. Statistical significance was determined at $P < 0.05$, unless otherwise indicated.

Mathematical model of the neuronal network

A Wilson-Cowan-like model, accounting for the spontaneous electrical activity observed in cultured neuronal networks, was defined and computer-simulated. It

aimed at supporting the interpretation of the *in vitro* recordings and at linking (phenomenologically) single-cell properties to spontaneously emerging network activity. The model describes at the population level, the instantaneous firing rates $\nu_{E1}(t)$, $\nu_{E2}(t)$ and $\nu_I(t)$ of a heterogeneous ensemble of excitatory (E) and inhibitory (I) neurons, respectively. Three populations were in fact considered (i.e. two excitatory and one inhibitory), each defined by a characteristic time scale (i.e. τ_E and τ_I), by single-cell *f-I* curve (i.e. $\phi(I_{syn})$) and by the specific recurrent connectivity [43,44,45,90].

$$\tau_E \frac{d\nu_{E1}}{dt} = -\nu_{E1} + \phi_{E1}(\mu_{E1}, \sigma_{E1})$$

$$\tau_E \frac{d\nu_{E2}}{dt} = -\nu_{E2} + \phi_{E2}(\mu_{E1} - g_{SFA}\, x_{SFA}\, \nu_{E2}, \sigma_{E2})$$

$$\tau_I \frac{d\nu_I}{dt} = -\nu_I + \phi_I(\mu_I, \sigma_I) \qquad (1)$$

The *f-I* curves were described by an identical transfer function of a *leaky Integrate-and-Fire* model neuron, expressed – under the hypotheses of the diffusion approximation [91]– by an analytical formula (see Supplemental Method). Here only the (infinitesimal) mean μ and variance σ^2 of the incoming average synaptic inputs are considered. These statistical parameters reflected the recurrent synaptic connectivity and of external inputs, as sketched in Fig. 5a, through the size of presynaptic populations (i.e. N_{ext}, N_{E1}, N_{E2}, N_I), the probability of recurrent connectivity (i.e. c), and the average of synaptic couplings (i.e. the charge associated to each postsynaptic potential; Δ_{EE}, Δ_{EI}, Δ_{IE}, Δ_{II}) and their standard deviations (i.e. $s\Delta_{EE}$, $s\Delta_{EI}$, $s\Delta_{IE}$, $s\Delta_{II}$)

$$\mu_{E1} = N_{ext}\Delta_{ext}\nu_{ext} + c\, N_{E1}\Delta_{EE}r_{E1}\nu_{E1} + c\, N_{E2}\Delta_{EE}r_{E2}\nu_{E2} + c\, N_I\Delta_{EI}\nu_I \qquad (2)$$

$$\mu_{E2} = N_{ext}\Delta_{ext}\nu_{ext} + c\, N_{E1}\Delta_{EE}r_{E1}\nu_{E1} + c\, N_{E2}\Delta_{EE}r_{E2}\nu_{E2} + c\, N_I\Delta_{EI}\nu_I$$

$$\mu_I = N_{ext}\Delta_{ext}\nu_{ext} + c\,N_{E1}\Delta_{IE}r_{E1}\nu_{E1} + c\,N_{E2}\Delta_{IE}r_{E2}\nu_{E2} + c\,N_I\Delta_{II}\nu_I$$

862

$$\begin{aligned}\sigma^2{}_{E1} &= N_{ext}(\Delta_{ext}^2 + s\Delta_{ext}^2)\nu_{ext} + c\,N_{E1}(\Delta_{EE}^2 + s\Delta_{EE}^2){r_{E1}}^2\nu_{E1} + c\,N_{E2}(\Delta_{EE}^2 \\ &\quad + s\Delta_{EE}^2){r_{E2}}^2\nu_{E2} + c\,N_I(\Delta_{EI}^2 + s\Delta_{EI}^2)\nu_I \\ \sigma^2{}_{E2} &= N_{ext}(\Delta_{ext}^2 + s\Delta_{ext}^2)\nu_{ext} + c\,N_{E1}(\Delta_{EE}^2 + s\Delta_{EE}^2){r_{E1}}^2\nu_{E1} + c\,N_{E2}(\Delta_{EE}^2 \\ &\quad + s\Delta_{EE}^2){r_{E2}}^2\nu_{E2} + c\,N_I(\Delta_{EI}^2 + s\Delta_{EI}^2)\nu_I \\ \sigma^2{}_{I} &= N_{ext}(\Delta_{ext}^2 + s\Delta_{ext}^2)\nu_{ext} + c\,N_{E1}(\Delta_{IE}^2 + s\Delta_{IE}^2){r_{E1}}^2\nu_{E1} + c\,N_{E2}(\Delta_{IE}^2 \\ &\quad + s\Delta_{IE}^2){r_{E2}}^2\nu_{E2} + c\,N_I(\Delta_{II}^2 + s\Delta_{II}^2)\nu_I\end{aligned} \quad (3)$$

863 Following closely [42], to approximately capture the dynamical filtering effects of
864 AMPAr- and GABAr-mediated synapses, each presynaptic mean firing rate ν in
865 equations. 4-5 was replaced by its low-passed version $\hat{\nu}$ which also included the
866 finite-size fluctuations [43]:

$$\begin{aligned}\tau_{AMPA}\frac{d\hat{\nu}_{E1}}{dt} &= -\hat{\nu}_{E1} + Poisson[N_{E1}\nu_{E1}\Delta t]/(N_{E1}\Delta t) \\ \tau_{AMPA}\frac{d\hat{\nu}_{E2}}{dt} &= -\hat{\nu}_{E2} + Poisson[N_{E1}\nu_{E1}\Delta t]/(N_{E1}\Delta t) \\ \tau_{GABA}\frac{d\hat{\nu}_{I}}{dt} &= -\hat{\nu}_{I} + Poisson[N_{E1}\nu_{E1}\Delta t]/(N_{E1}\Delta t)\end{aligned} \quad (4)$$

867 where, for each time *t*, $Poisson[x]$ indicates a new realization of a pseudo-random
868 number, drawn form a Poisson distribution with mean x, and where Δt is the
869 numerical integration step.
870 The effects of homosynaptic short-term depression at excitatory synapses and spike
871 frequency adaptation in just one of the two excitatory populations, were finally
872 described by three additional equations

$$\tau_{SFA}\frac{dx_{SFA}}{dt} = -x_{SFA} + \ Poisson[N_{E1}\nu_{E1}\Delta t]/(N_{E1}\Delta t)$$

$$\tau_{STD}\frac{dr_{E1}}{dt} = 1 - r_{E1} \ - \ U \ r_{E1}\,\tau_{STD}\,\hat{v}_{E1}$$

$$\tau_{STD}\frac{dr_{E2}}{dt} = 1 - r_{E2} \ - \ U \ r_{E2}\,\tau_{STD}\,\hat{v}_{E2} \qquad (5)$$

and by replacing including short-term synaptic depression, intrinsic spike frequency adaptation, and the effects to the finite size of the network [43].

Model parameter	**Value**
$N_{E1} + N_{E2}$	1280
N_I	400
τ_E	20 ms
τ_I	20 ms
τ_{AMPA}	10 ms
τ_{GABA}	2 ms
τ_{STD}	800 ms
τ_{SFA}	1500 ms
g_{SFA}	10 a.u.
U	0.2
$\Delta_{ext} \pm s\Delta_{ext}$	(0.416 $\pm$ 0.104) / C_m mV
$\Delta_{EE} \pm s\Delta_{EE}$	(0.809 $\pm$ 0.202) / C_m mV
$\Delta_{EI} \pm s\Delta_{EI}$	(-0.34 $\pm$ 0.085) / C_m mV
$\Delta_{IE} \pm s\Delta_{IE}$	(1.23 $\pm$ 0.307) / C_m mV
$\Delta_{II} \pm s\Delta_{II}$	(-0.358 $\pm$ 0.0894) / C_m mV
$N_{ext}\nu_{ext}$	1.25 kHz
c	0.25
C_m	20 pF
R_m	1 $k\Omega$
E_m	-70 mV
V_θ	-55 mV
V_H	-70 mV
τ_{arp}	2 ms

Table 1: Numerical values employed in the simulations of Figure 5.

Additional details are provided in Supplemental materials and full model details and the source code are provided as a ModelDB entry [92].

(https://senselab.med.yale.edu/ModelDB; accession number 230930, temporary password 1234).

Conductance based model

A minimal model of neuronal excitability was considered by studying the classic single-compartmental conductance-based description proposed by Hodgkin and Huxley (1952). Therein, the electrical potential *V* across the cell membrane, satisfies the conservation of charge

$$C_m \frac{dV}{dt} = I_{Na} + I_K + I_{leak} + I_{stim}$$

where the sum of externally applied currents (I_{stim}), capacitive displacement currents ($C_m dV/dt$), and ionic transport currents across the membrane (I_{Na}, I_K, I_{leak}) are always balanced. The model is completely described by additional three state variables (i.e. *m, h, n*), expressing the voltage- and time-dependent fractions of inward and outward ionic currents, $I_{Na} = G_{Na} m^3 h\,(E_{Na} - V)$, $I_K = G_K n^4\,(E_K - V)$, $I_{leak} = G_{leak}\,(E_{leak} - V)$ as a first-order kinetic process:

$$\frac{dx}{dt} = \alpha_x\,(1 - x) - \beta_x\,x \text{ , with } x \in \{m, h, n\}$$

Model parameters are indicated in Table 1, unless noted otherwise.

Parameter	Description	Value
C_m	*Specific cell capacitance*	0.01 μF/mm^2
E_{Na}	*Nernst potential for Na^+ ions*	30 mV
E_K	*Nernst potential for K^+ ions*	-75 mV
E_{leak}	*Nernst potential for "leak" ionic currents*	-80 mV
G_{Na}	*Maximal conductance for Na^+ ions*	0.333 mS/mm^2
G_K	*Maximal conductance for K^+ ions*	0.012 mS/mm^2
G_{leak}	*Maximal conductance for "leak" currents*	0.003 mS/mm^2
I_{stim}	*External DC current stimulus amplitude*	15 nA/mm^2
$\alpha_m(V)$	*Kinetic rate of Na^+ current activation*	0.1 F(0.1,V+35)
$\beta_m(V)$	*Kinetic rate of Na^+ current activation*	4 exp(-(V+60)/18) ms
$\alpha_h(V)$	*Kinetic rate of Na^+ current inactivation*	0.07 exp(-(V+60)/20) ms
$\beta_h(V)$	*Kinetic rate of Na^+ current inactivation*	[exp(-(V+30)/10)+1]$^{-1}$ ms
$\alpha_n(V)$	*Kinetic rate of K^+ current activation*	0.01 F(0.1,V+50) ms
$\beta_n(V)$	*Kinetic rate of K^+ current activation*	0.125 exp(-(V+60)/80) ms

F(x,y)	*Boltzman sigmoid function*	y / [1 - exp(x * y)] ms
Δt	Numerical solution time-step	0.001 ms

Table 2 – Parameters employed in the simulations of the Hodgkin-Huxley (HH) model. The standard HH mathematical model was numerically simulated as a minimal description of neuronal excitability to gain insight on current-clamp experimental recordings.

FIGURE LEGENDS

Figure 1 | Characterization of the substrates. a, AFM topography reconstructions of glass control, SLG, MLG and gold plated glass surfaces. Scale bar: 5 μm. **b**, Spatial maps of the 2D/G and D/G peak amplitude ratio maps. Scale bar: 10 μm. The single punctual Raman spectra of SLG (in red) and MLG (in blue) represent mapping data points with the corresponding average peak amplitude ratios. To the right, relative spatial 2D/G and D/G ratio maps. **c**, XPS spectrum (X-Ray source: Mg Kα) of SLG (in red) and MLG (in blue). Dotted lines highlight the relevant elements, while the unlabeled features around 750 eV and 980 eV correspond to the oxygen KL_1L_1 and the carbon KVV Auger lines respectively.

Figure 2 | Single-Layer graphene increase neuronal network activity. a, Representative SEM micrographs depicting hippocampal neuron morphology after 10 DIV-growth supported by the different substrates. Scale bar: 10 μm. **b**, Representative fluorescent microscopy images showing dissociated hippocampal networks labeled with class III β-tubulin (for neurons) in red and GFAP (for astrocytes) in green. Scale bar: 100 μm. Cultures grown on the different materials

displayed a comparable number of cells, quantified as DAPI-positive nuclei (upper right histograms) and a similar fraction of glial and neuronal cells (lower right histograms). **c**, Representative traces of the spontaneous network activity of neurons grown on the different substrates are shown (left), the corresponding isolated PSCs are shown superimposed (middle; in black the average values). Box plots summarize the PSC amplitude values (right, top) and the PSC frequency ones (right, bottom) in all experimental conditions. Note the significant increase in PSC frequency in SLG when compared to all the other substrates.

Figure 3 | Single-layer graphene does not increase the number of synapses and the network composition. a, Exemplificative spontaneous traces of synaptic activity recorded in the presence of TTX are shown together with their superimposed mPSCs (right, in black the average values); Control and SLG mPSC frequency and amplitude are summarized in the box plots, note that no differences were detected in these parameters. **b**, Confocal images of neuronal cultures (10 DIV) in Control and SLG identifying the presynaptic VGlut1 (in green) in III β-tubulin positive cells (orange). Scale bar: 20 μm. Higher magnifications of the region highlighted by white boxes are displayed for clarification. Scale bar: 5 μm. The histograms summarize VGlut1 puncta densities in the two conditions (right). **c**, Confocal images of neuronal cultures (10 DIV) in Control and SLG identifying positive cells for class III β-tubulin and GABA. Scale bar: 10 μm. The histograms summarize the percentage of double-positive cells in the two conditions (right).

Figure 4 | SLG triggers changes in single cell intrinsic excitability. a, Current-clamp recordings of hippocampal neurons in culture (10 DIV) in Control and SLG.

944 The spontaneous occurrence of APs is summarized in the histograms (right). Note
945 the significant increase of AP frequency in SLG. **b**, Evoked single AP in Control (top)
946 and SLG (bottom). Note the pronounced AHP in SLG neurons, that was partially
947 abolished by each of the treatments shown, BaCl, TEA or Apamin (right,
948 superimposed tracings). The histogram quantifies the area below the Control and
949 SLG post-AP voltage trajectories with respect to the resting membrane potential. **c**,
950 Current-clamp recordings from hippocampal neurons in control and SLG induced
951 different discharge patterns that identified two cell categories: *Adapting or Tonic*. **d**,
952 Bar charts illustrate probability distributions (expressed as percentage of sampled
953 population) of each cell type in control and SLG cultures. **e**, Scatter plot of after-
954 potential area *vs*. the number of action potentials (APs) in SLG neurons when a
955 single AP is elicited (as in b; open circle) or when multiple APs are evoked (as in c,
956 filled circle) by 1 s long depolarizing step **f**, Representative records of voltage-
957 activated outward currents evoked by depolarizing current steps in control and SLG
958 (capacitive transients were not removed). Plot summarizes the I/V relation in control
959 and SLG neurons obtained upon subtraction of leak currents. Note that SLG outward
960 currents were significantly larger than control ones.
961
962 **Figure 5 | Spike-rate "extended mean-field" model.** The model, describing
963 mathematically the electrical activity of excitatory and inhibitory recurrently
964 interacting neurons, was defined and computer simulated (see Supplemental
965 Methods). **a**, The increase in the fraction of non-adapting neurons, observed *in vitr*o
966 on graphene substrates, predicts *in silic*o a higher rate of occurrence for
967 spontaneous synchronized "bursts" of spikes across the entire network. These bursts
968 are presynaptic correlates of the spontaneous compound synaptic potentials,

observed experimentally by voltage-clamp. **b** and **c**, Samples of the simulated time series, analysed in **a**, are shown for two values of the fraction of non-adapting neurons, *i.e.* 20% and 80%, out of the total of excitatory neurons. **d**, A counter-intuitive effects of outward potassium currents on cell excitability are explored in a minimal mathematical model. The Hodgkin-Huxley model was numerically integrated (parameters as in Table 2) to simulate membrane potential responses (black traces) to an external step current comparable to experiments (see Methods). **d** and **e**, Plots within each panel exemplify how an increase (from left subpanels to right subpanels) of the maximal K^+ conductance or, in **f**, its driving force, through a depletion of extracellular K^+ ions, may to some extent reverse the progressive inactivation of inward Na^+ currents (green traces in **d**). Then, inactivating neuronal responses may turn into sustained firing thereby increasing cell excitability (as in **c**). Parameters: in **d**, G_K in {0.012; 0.0216} mS/mm^2; in **e**, G_K in {0.012, 0.04, 0.06} mS/mm^2 from left to right, I_{stim} 5 nA/mm^2; in **f**, I_{stim} as in **e**, while E_K in {-75, -77.6, -80.5} mV from left to right, corresponding to a {0%, 10%, 20%} depletion of extracellular K^+ ions.

Figure 6 | Graphene deplete potassium at the cell/substrate cleft. a, The Raman spectra of graphene G band in wet condition are shown for SLG (left) and MLG (right). Control condition (D_2O, in black) is compared with spectra of graphene immersed in 4 mM D_2O solution (in red) of KCl and 150 mM solution of NaCl (in green). Note that high concentrated NaCl induce in SLG a smaller shift in G-Peak position than KCl while no shifts are detectable in MLG as outlined in the insets. **b**, Sketch of the local amount of K^+ depletion in the membrane/surface cleft due to graphene trapping as function of cleft thickness. In light green the extrapolated values of such a distance (40-100 nm) [46]. **c**, Box plots summarize the average

PSC frequency values (left) and the average PSC amplitudes ones (right) for neurons developed on glass control (in grey), on glass supported SLG (in red), on free-standing SLG (in green) and on SLG deposited on ITO (in blue). Note the significant increase in PSC frequency in SLG laying on insulating glass or, even more, when grown on suspended SLG. SLG on conductive ITO does not change neuronal activity. **d**, Hypothesis of Dirac point and Fermi level rearrangement as function of SLG supporting material (bottom), and an exemplification of the possible charge distribution in graphene layer as function of electrical characteristics of the underlying surface (top). Blue areas represent more positive regions (e.g. depletion of electrons), red areas represent more negative ones (e.g. persistency of electrons).

REFERENCES

[1] Novoselov, K. S. et al. Electric Field Effect in Atomically Thin Carbon Films. Science 306, 666-669 (2004).

[2] Geim, A. K. & Novoselov, K. S. The rise of graphene. Nat Mater. 6, 183-191 (2007).

[3] Yang, Y. et al. Graphene based materials for biomedical applications. Mat Today 16, 365-373 (2013).

[4] Li, X., et al. Transfer of large-area graphene films for high-performance transparent conductive electrodes. Nano Letters 9, 4359-4363 (2009)

[5] Shin, S. R. et al. Graphene-based materials for tissue engineering. Adv Drug Deliv Rev. 105, 255-274 (2016).

[6] Lu, Y. et al. Flexible Neural Electrode Array Based-on Porous Graphene for Cortical Microstimulation and Sensing. Sci Rep. 6, 33526 (2016).

[7] Herbert, C. et al. Flexible graphene solution-gated field effect transistors, efficient transducers for micro-electrocorticography Adv. Funct. Mater.1703976 (2017).

[8] Kim, J. et al. Monolayer Graphene-Directed Growth and Neuronal Differentiation of Mesenchymal Stem Cells. J Biomed Nanotechnol. 11, 2024-2033 (2015).

[9] Fabbro, A. et al. Graphene-Based Interfaces Do Not Alter Target Nerve Cells. ACS Nano 10, 615-623 (2016).

[10] Rauti, R. et al. Graphene Oxide Nanosheets Reshape Synaptic Function in Cultured Brain Networks. ACS Nano 10, 4459-4471 (2016).

[11] Famm, K. et al. Drug discovery: a jump-start for electroceuticals. Nature 496, 159-161 (2013).

[12] Rivnay, J. et al. Next-generation probes, particles, and proteins for neural interfacing. Sci Advances 3, e1601649 (2017).

[13] Li, X. et al. Large-area synthesis of high-quality and uniform graphene films on copper foils. Science. 324, 1312-4 (2009).

[14] Cançado, L.G. et al. Quantifying defects in graphene via Raman spectroscopy at different excitation energies. Nano lett. 11, 3190-3196 (2011).

[15] Ferrari A. C. et al. Raman spectrum of graphene and graphene layers. Phys. Rev. Lett. 97, 187401 (2006).

[16] Cançado, L. G. et al. Measuring the degree of stacking order in graphite by Raman spectroscopy. Carbon 46, 272-275 (2008).

[17] Lovat, V. et al. Carbon nanotube substrates boost neuronal electrical signaling. Nano lett. 5, 1107-1110 (2005).

[18] Cellot, G. et al. Carbon nanotubes might improve neuronal performance by favouring electrical shortcuts. Nat. Nanotechnol. 4, 126-133 (2009).

[19] Cellot, G. et al, Carbon nanotube scaffolds tune synaptic strength in cultured neural circuits: novel frontiers in nanomaterial-tissue interactions. J. Neurosci. 31, 12945-12953 (2011).

[20] Kim, J. et al, Monolayer Graphene-Directed Growth and Neuronal Differentiation of Mesenchymal Stem Cells. J Biomed. Nanotechnol. 11, 2024-2033 (2015).

[21] Baldrighi, M. et al, Carbon Nanomaterials Interfacing with Neurons: An In vivo Perspective. Front. Neurosci. 10, 260 (2016).

[22] Pampaloni, NP. et al. Sculpting neurotransmission during synaptic development by 2D nanostructured interfaces. Nanomedicine. doi: 10.1016/j.nano.2017.01.020.

[23] Raastad, M. et al. Putative Single Quantum and Single Fibre Excitatory Postsynaptic Currents Show Similar Amplitude Range and Variability in Rat Hippocampal Slices. Eur J Neurosci. 4, 113-117 (1992).

[24] Arosio, D. & Ratto, GM. Twenty years of fluorescence imaging of intracellular chloride. Front Cell Neurosci. 8, 258 (2014).

[25] Cherubini, E. GABA mediated excitation in immature rat CA3 hippocampal neurons. Int J Dev Neurosci. 8, 481-90 (1990).

[26] Marandi, N., Konnerth, A. & Garaschuk O. Two-photon chloride imaging in neurons of brain slices. Pflugers Arch. 445, 357-65 (2002).

[27] Ruscheweyh, R. & Sandkuhler, J. Lamina-specific membrane and discharge properties of rat spinal dorsal horn neurones in vitro. J Physiol. 541, 231-244 (2002).

[28] Chang, YM. & Luebke, JI. Electrophysiological diversity of layer 5 pyramidal cells in the prefrontal cortex of the rhesus monkey: in vitro slice studies. J Neurophysiol. 98, 2622-32. (2007)[29] Routh, B. N. et al. Anatomical and Electrophysiological Comparison of CA1 Pyramidal Neurons of the Rat and Mouse. J Neurophysiol. 102, 2288–2302 (2009).

[30] Renganathan, M., Cummins, TR. & Waxman, SG. Contribution of Na(v)1.8 sodium channels to action potential electrogenesis in DRG neurons. J Neurophysiol. 86, 629-40 (2001).

[31] Platkiewicz, J. & Brette, R. Impact of Fast Sodium Channel Inactivation on Spike Threshold Dynamics and Synaptic Integration. PLoS Comput Biol. 7, e1001129 (2011).

[32] Kress, G. J. et al. Axonal sodium channel distribution shapes the depolarized action potential threshold of dentate granule neurons. Hippocampus 20, 558-571 (2016).

[33] Alagem, N. et al, Mechanism of Ba(2+) block of a mouse inwardly rectifying K+ channel: differential contribution by two discrete residues. J Physiol. 534, 381-393 (2001).

[34] Alger, B. E. & Nicoll, R. A. Epileptiform burst afterhyperolarization: calcium-dependent potassium potential in hippocampal CA1 pyramidal cells. Science 210, 1122-1124 (1980).

[35] Jiang, Y. & MacKinnon, R. The barium site in a potassium channel by x-ray crystallography. J Gen Physiol. 115, 269-272 (2000).

[36] Nisenmbaum, E. S. & Wilson, C. J. Potassium currents responsible for inward and outward rectification in rat neostriatal spiny projection neurons. J Neurosci. 15, 4449-4463 (1995).

[37] Storm, J. F. Action potential repolarization and a fast after-hyperpolarization in rat hippocampal pyramidal cells. J Physiol. 385, 733-759 (1987).

[38] Pisirowski, R. & Aldrich, R. W. Calcium activation of BK(Ca) potassium channels lacking the calcium bowl and RCK domains. Nature 420, 499-502 (2002).

[39] Stocker, M. et al, An apamin-sensitive Ca2+-activated K+ current in hippocampal pyramidal neurons. Prot Nat Acad Sci. 96, 4662-4667(1999).

[40] Sah, P. & Faber, E. S. Channels underlying neuronal calcium-activated potassium currents. Prog Neurobiol. 66, 345-353 (2002).

[41] Dégenètais, E. et al. Electrophysiological properties of pyramidal neurons in the rat prefrontal cortex: an in vivo intracellular recording study. Cereb Cortex 12, 1-16 (2002).

[42] Furlan, F. et al. ERG conductance expression modulates the excitability of ventral horn GABAergic interneurons that control rhythmic oscillations in the developing mouse spinal cord. J. Neurosci. 27, 919-928 (2007).

[43] Gigante, G. et al. Network Events on Multiple Space and Time Scales in Cultured Neural Networks and in a Stochastic Rate Model. PLoS Comput Biol. 11, e1004547 (2015).

[44] Gambazzi, L. et al. Diminished activity-dependent brain-derived neurotrophic factor expression underlies cortical neuron microcircuit hypoconnectivity resulting from exposure to mutant huntingtin fragments. J. Pharmacol Exp Ther. 335, 13-22 (2010).

[45] Giugliano, M. et al. Single-neuron discharge properties and network activity in dissociated cultures of neocortex. J Neurophysiol. 92, 977-996 (2004).

[46] Marom, S. & Shahaf, G. Development, learning and memory in large random networks of cortical neurons: lessons beyond anatomy. Q Rev Biophys. 35, 63-87 (2002).

[47] Hodgkin, A. L. & Huxley, A. F. A quantitative description of membrane current and its application to conduction and excitation in nerve. J Physiol. 117, 500-544 (1952).

[48] French, C. R. et al. Properties of an intermediate-duration inactivation process of the voltage-gated sodium conductance in rat hippocampal CA1 neurons. J Neurophysiol. 115, 790-802 (2016).

[49] Fleidervish, IA & Gutnick, MJ. Kinetics of slow inactivation of persistent sodium current in layer V neurons of mouse neocortical slices. J Neurophysiol. 76, 2125-30 (1996).

[50] Miles, GB., Dai, Y. & Brownstone, RM. Mechanisms underlying the early phase of spike frequency adaptation in mouse spinal motoneurones. J Physiol. 566, 519–532 (2005).

[51] Sterratt, D. Principles of computational modelling in neuroscience. Cambridge University Press(2011).

[52] Kumpf R A, & Dougherty D A. A mechanism for ion selectivity in potassium channels: computational studies of cation-pi interactions. Science. 261, 1708-10 (1993).

[53] Shi, G,et al. Ion enrichment on the hydrophobic carbon-based surface in aqueous salt solutions due to cation-π interactions. Sci Rep., 3, 3436 (2013).

[54] Pham T A, et al. Salt Solutions in Carbon Nanotubes: The Role of Cation−π Interactions J. Phys. Chem. C, 120,7332–7338 (2016).

[55] Williams, C D, et al. Effective Polarization in Pairwise Potentials at the Graphene–Electrolyte Interface J. Phys. Chem. Lett., 8,703–708 (2017)

[56] Dong, X et al. Doping single-layer graphene with aromatic molecules. Small. 5,1422-6 (2009)

[57] Chacón-Torres, JC, Wirtz, L, Pichler, T. Manifestation of charged and strainedgraphene layers in the Raman response of graphite intercalation compounds. ACS Nano. 7, 9249-59 (2013).

[58] Spira ME, Hai A. Multi-electrode array technologies for neuroscience and cardiology. Nat Nanotechnol. 8,83-94 (2013).

[59] Son, IH., et al. Graphene balls for lithium rechargeable batteries with fast charging and high volumetric energy densities. Nat comm. 8, 1561 (2017).

[60] Baronsky, T., et al. Cell-Substrate Dynamics of the Epithelial-To-Mesenchymal Transition. Nano Lett. 17, 3320-3326 (2017).[61] Pestova, O.N.et al. X-ray Phase Analysis of Structure of Water-Salt Systems: NaCl-H2O and KCl-H2O. Russian J of Appl Chem. 77,1066-1069 (2004)

[62] Novák M, et al. Solvent effects on ion-receptor interactions in the presence of an external electric field. Phys Chem Chem Phys. 18,30754-30760 (2016).

[63] Chen, K. et al, Electronic Properties of Graphene Altered by Substrate Surface Chemistry and Externally Applied Electric Field. J. Phys. Chem. C,, 116,6259–6267 (2012)

[64] Novoselov, K. et al., Two-dimensional gas of massless Dirac fermions in graphene. Nature.438, 197-200 (2005).

[65] González-Herrero, H et al. Graphene Tunable Transparency to Tunneling Electrons: A Direct Tool To Measure the Local Coupling. ACS Nano. 10,5131-44 (2016).

[66] Praveen, C. S. et al., Adsorption of alkali adatoms on graphene supported by the Au/Ni(111) surface, Phys Rev. B 92, 075403 (2015).

[67] Kang, Y-J. et al. Electronic structure of graphene and doping effect on SiO2 Phys Rev. B 78, 115404 (2008).

[68] Miwa, R. H. et al. Doping of graphene adsorbed on the a-SiO2 surface.Appl Phys Lett99, 163108 (2011).

[69] Ao, Z. et al. Density functional theory calculations on graphene/α-SiO2(0001) interface. Nanoscale Res Lett. 7,158 (2012).

[70] Fan, X. F. et al. Interaction between graphene and the surface of SiO2. J Phys Condens Matter. 24:305004 (2012).

[71] Terrones, M., et al. Graphene and graphite nanoribbons: Morphology, properties, synthesis, defects and applications. Nano Today, 5,351-372 (2010).

[72] Nezich, D. et al. Electrical characterization of graphene synthesized by chemical vapor deposition using Ni substrate. Nanotechnology 23, 015701 (2012).

[73] Hille, B. Ion channels of excitable membranes. Sunderland, Mass: Sinauer, (2001).

[74] Slomowitz, E. et al. Interplay between population firing stability and single neuron dynamics in hippocampal networks. eLife 4: e04378 (2015).

[75] Bogaard, A. et al. Interaction of cellular and network mechanisms in spatiotemporal pattern formation in neuronal networks. J Neurosci. 29, 1677-1687 (2009).

[76] Sahasranamam, A. et al. Dynamical state of the network determines the efficacy of single neuron properties in shaping the network activity. Sci Rep. 6, 26029 (2016).

[77] Radulescu, R.A. Mechanisms Explaining Transitions between Tonic and Phasic Firing in Neuronal Populations as Predicted by a Low Dimensional Firing Rate Model. PLoS One 5:e12695 (2010).

[78] Naud, R. et al. Firing patterns in the adaptive exponential integrate-and-fire model. Biol Cybern. 99, 335-347 (2008).

[79] Wrobel G, Höller M, Ingebrandt S, Dieluweit S, Sommerhage F, Bochem HP, Offenhäusser A. Transmission electron microscopy study of the cell-sensor interface. J R Soc Interface. 5, 213-222. (2008).

[80] Braun, D. & Fromherz, P. Fluorescence interference-contrast microscopy of cell adhesion on oxidized silicon. Appl Phys A 65: 341-348 (1997).

[81] Nicholson, C, Phillips, J. M. Ion diffusion modified by tortuosity and volume fraction in the extracellular microenvironment of the rat cerebellum. J Physiol. 321, 225-57 (1981).

[82] Usmani S, et al. 3D meshes of carbon nanotubes guide functional reconnection of segregated spinal explants. Sci Adv. e1600087 (2016).

[83] Drieschner, S. et al. Frequency response of electrolyte-gated graphene electrodes and transistors. Journal of Physics D: Applied Physics 50, 095304 (2017).

[84] Drieschner, S. et al. High surface area graphene foams by chemical vapor deposition. 2D Materials 3, 045013 (2016).

[85] Matruglio, A. et al. Contamination-free suspended graphene structures by a Ti-based transfer method Carbon, 103, 305-310 (2016).

[86] Clements, J. D. & Bekkers, J. M. Detection of spontaneous synaptic events with an optimally scaled template. Biophys J. 73, 220-229 (1997).

[87] Sontheimer, H. & Ransom, C. Whole-Cell Patch-Clamp Recordings. Neuromethods 35, 35-67 Humana Press Inc., (2007).

[90] La Camera G, et al The response of cortical neurons to in vivo-like input current: theory and experiment: I. Noisy inputs with stationary statistics. Biol Cybern 99:279–301(2008).

[91] Ricciardi, L. M. Diffusion Processes and Related Topics in Biology. Lecture notes in Biomathematics. Springer-Verlag (1977).

[92] Hines, M. L. et al. Model DB: A Database to Support Computational Neuroscience. J Comput Neurosci. 17, 7-11 (2004).

[93] Gertler, T. S., Chan, C.S., Surmeier, D.J. Dichotomous anatomical properties of adult striatal medium spiny neurons. J Neurosci. 28, 10814-10824 (2008).

Acknowledgement

We are grateful to M. Lazzarino and S. Dal Zilio for experimental assistance in the fabrication of suspended SLG and FIB analysis; N. Secomandi and R. Rauti for assistance in imaging. We thank A. Laio, G. Scoles, A. Nistri and B. Cortés-Llanos for helpful discussion. This paper is based on work supported by the European Union Seventh Framework Program under grant agreement no. 696656 Graphene Flagship and by the Flanders Research Foundation (grant no. G0F1517N). MP, as the recipient of the AXA Chair, is grateful to the AXA Research Fund for financial support. MP was also supported by the Spanish Ministry of Economy and Competitiveness MINECO (project CTQ2016-76721-R),

by the University of Trieste and by Diputación Foral de Gipuzkoa program Red (101).

Contributions

N.P.P. performed electrophysiological experiments, imaging, immunochemistry, confocal microscopy and all the related analysis; M.L. fabricated supported SLG and MLG and performed all material characterization; M.G. performed mathematical simulations and analysis and contributed to the writing of the manuscript; A.M. fabricate suspended SLG and gold plated samples; F.D.A. and A.M. performed Raman experiments and data analysis on SLG and MLG in wet and dried conditions; M. P., D.S. and L.B. conceived the study; D.S., L.B., and J.A.G. designed the experimental strategy, interpreted the results and wrote the manuscript.

Additional information

Supplementary information is available in the online version of the paper.

Correspondence and requests for materials should be addressed to Denis Scaini dscaini@sissa.it; Josè Antonio Garrido joseantonio.garrido@icn2.cat; Laura Ballerini laura.ballerini@sissa.it

Competing financial interests

The authors declare no competing financial interests.

Data availability

All the data that support the findings of this study are available within the article and in its Supplementary Information, and these data are available from the corresponding author on request.

SUPPLEMENTARY INFORMATION

Supplemental methods in neuronal network simulation

In our numerical simulations of a networks of interacting excitatory and inhibitory neurons, the electrical response properties of each cell are approximated by those of a *leaky* Integrate-and-Fire unit. In this model, characterized by a lumped membrane capacitance C_m and R_m, the membrane potential of the neuron *V(t)* passively integrates incoming synaptic input currents I_{syn}, around a resting membrane potential E_m and while below the excitability threshold V_θ:

$$C_m \frac{dV}{dt} = \frac{(E_m - V)}{R_m} + I_{syn} \qquad V < V_\theta \tag{S1}$$

As *V* reaches V_θ, the unit is said to *fire* a spike and *V* is reset and hold to a hyperpolarized voltage V_H, for the entire duration of an absolute refractory period τ_{arp}:

$$V(t^*) = V_\theta \qquad V(t) \to V_H \;\; t \in (t^*;\, t^* + \tau_{arp}] \tag{S2}$$

Synaptic interactions are described as current-driven impulsive inputs, where a (train of) presynaptic spike occurring at time t_k is received postsynaptically as a (train of) Dirac's Delta function with a net charge of Δ:

$$I_{syn} = \sum_k \Delta\, \delta(t - t_k) \tag{S3}$$

When the occurrence times $\{t_k\}$ are statistically independent and occurring as stochastic Poisson-distributed events with mean frequency λ, the mean spiking rate ν of a generic unit of the network can be approximated by an analytical expression (90) that is valid as long as λ is very large and Δ is very small (i.e. while the product $\lambda\Delta$ remains finite):

$$\nu = \phi(\mu, \sigma) = [\tau_{arp} + R_m C_m \int_A^B \sqrt{\pi} e^{x^2} (1 + \mathrm{erf}(x)) dx]^{-1} \quad \text{(S4)}$$

where $A = \frac{V_\theta - E_m - R_m \mu}{\sigma \sqrt{R_m / C_m}}$ and $B = \frac{V_H - E_m - R_m \mu}{\sigma \sqrt{R_m / C_m}}$, with $\mu = \Delta\, \lambda$ and $\sigma = \Delta \sqrt{\lambda}$.

This expression can be included in a rate-based model, where the activity of individual units is however accounted for implicitly: if synaptic inputs can be considered as statistically identical, then only one equation can be used for describing the evolution in time of the

$$\tau \frac{dv}{dt} = -\nu + \phi(\mu, \sigma) \quad \text{(S5)}$$

Supplemental technical details about the Raman set-up

In order to compare cation/graphene interaction in SLG and MLG in an environment close to the one where neurons were investigated, we decided to acquire the Raman spectra from samples maintained under liquid conditions. To that aim, samples were kept in a liquid cell and were covered by a thin layer of liquid solution (0.5-1 mm in thickness; Supplementary Fig. 5a) during the whole measurement process. The experiments were performed using a Raman scattering set-up that required keeping the sample surface perpendicular to the ground. Since this procedure would not allow measuring the samples while immersed in liquids, a technical modification of the set-up has been employed. More specifically (Supplementary Fig. 5a), a 45° mirror has been included in the set-up that allowed placing the sample horizontally inside a liquid cell, enabling ease liquid exchange during experiments. Thus, SLG and MLG samples were fully cover by liquid during the entire measurements, providing more representative conditions. The use of a macro-spot (about 100 µm in

diameter) in the Raman set-up limits the occurrence of molecular fluctuations –due to a thermal effect induced by laser focusing– that may alter the measurements.

Supplementary Figure 1 a, Box plots summarizing the average PSC frequency values (left) and the average PSC amplitudes ones (right) for neurons developed on supported SLG transferred using PMMA (in grey), or PS (in red). SLG induce in neurons' PSCs similar effects when the carbon film is transferred through PMMA or PS. **b**, Offline differential analysis of PSC decays (τ) identifies fast and slow events (inset, average tracings from a representative SLG neuron). Bar plot summarizes the frequency of fast and slow PSCs in Controls and SLG.

Supplementary Figure 2 a, Snapshot of MQAE-loaded hippocampal neurons (9 DIV) in Control and SLG. Scale bars 15 μm. Changes in fluorescence represent opposite directions of GABA evoked Cl^- fluxes caused by 500 ms long pressure applications of GABA (middle tracings, 2 different cells). Note the absence of fluorescence changes when 500 ms long pressure standard saline solution (Saline) were applied. Bar plot summarizes the percentage of cells responding with a Cl^- influx (in blue) or efflux (in red) in Control and SLG. **b**, NKCC1 is expressed on hippocampal neurons in Control and SLG. Confocal images of neuronal cultures (9 DIV) in Control and SLG demonstrate NKCC1 (in green) in class III β-tubulin positive cells (in red). Scale bar: 30 μm. Merged images are displayed for clarification. Scale bar: 30 μm. The histograms summarize NKCC1 volume normalized to class III β-tubulin volume in the two conditions (right; n= 20 each).

Supplementary Figure 3 Firing patterns evoked in Control and SLG neurons by near-threshold current steps. **a.** APs were elicited by 200 ms current steps of 40 pA (blue traces) and 60 pA (orange traces) amplitudes in control (n = 5) and SLG (n = 5) neurons kept at -60 mV membrane potential. Plot in **b.** shows that SLG neurons usually fire more APs at near-threshold (60 pA) current injections with respect to Controls. The estimated rheobase current values [93] did not differ in these two groups of neurons (56.5 ± 12.9 pA and 60.5 ± 12.8 pA, control and SLG neurons respectively).

Supplementary Figure 4 The mathematical model of neuronal excitability considered in the paper was systematically explored testing the robustness of our conclusions. The space of parameters, represented by the ionic maximal conductances for sodium and potassium channels, was considered and subdivided in regions with transient (black) and sustained (white) firing responses. Increasing inward currents by the value of sodium maximal conductances obviously increases excitability: i.e. moving *from left to right while in the dark brings to the white peninsula*. However, there is a wide portion of the plane where increasing outward currents by the value of potassium maximal conductances also increases excitability: i.e. moving *from bottom to top while in the dark brings to the peninsula.* The transition of neuronal phenotype, observed comparing control and SLG conditions (Fig. 4c), resembles more the latter than the former case. Parameters: G_K in [0.02; 0.11] mS/mm^2, G_{Na} in [0.01; 0.91] mS/mm^2, I_{stim} 20 nA/mm^2.

Supplementary Figure 5 a, Schematic representation of the technical modifications adopted in the standard backscattering Raman set-up to allow measurements taking

advantage of a liquid cells to obtain graphene Raman spectra in genuine liquid conditions. **b**, SLG Raman spectra of G band in dry condition (e.g. after samples were carefully rinsed with D_2O and let dry in a N_2 box for 1 hour). Control condition (air, in black) is compared with spectra of graphene previously immersed in 4 mM D_2O of KCl (in red) and 150 mM solution of NaCl (in green). Note that, differently from the wet experiments depicted in Figure 6a, NaCl induce now in SLG a larger shift in G-Peak position than KCl (see inset).

Supplementary Figure 6 a, SEM image of a neuronal cell developed above a glass substrate. The white arrow indicates the cell region where focused ion beam (FIB) was used to obtain a cell cross section. **b,** SEM magnification of the milled cell portion. The image points out the presence of a gap between the cell process and the glass substrate (brighter region of electron accumulation) of about hundreds of nm, presumably filled with extracellular matrix and solution. **c,** A cartoon pointing out the different components visible in the cross section. Interestingly, the gap appears variable in its extent: larger centrally and smaller at the edges. **d**, SEM image of a neuronal cell developed above SLG. The arrow indicates the milled cell region. **e,** SEM image pointing out the presence of a similar gap between the cell process and the substrate of nearly one hundred of nm. The thin single layer of graphene, a fraction of nm in thickness, is not detectable but the underneath supporting glass is clearly visible (brighter region of electron accumulation). The cell/substrate distance appears smaller than on control glass. **f,** A cartoon pointing out the different components visible in the cross section. Lateral cellular or extracellular patches seem partially closing the gap. Scale bars are 5 μm in a and d; 200 nm in b and e.

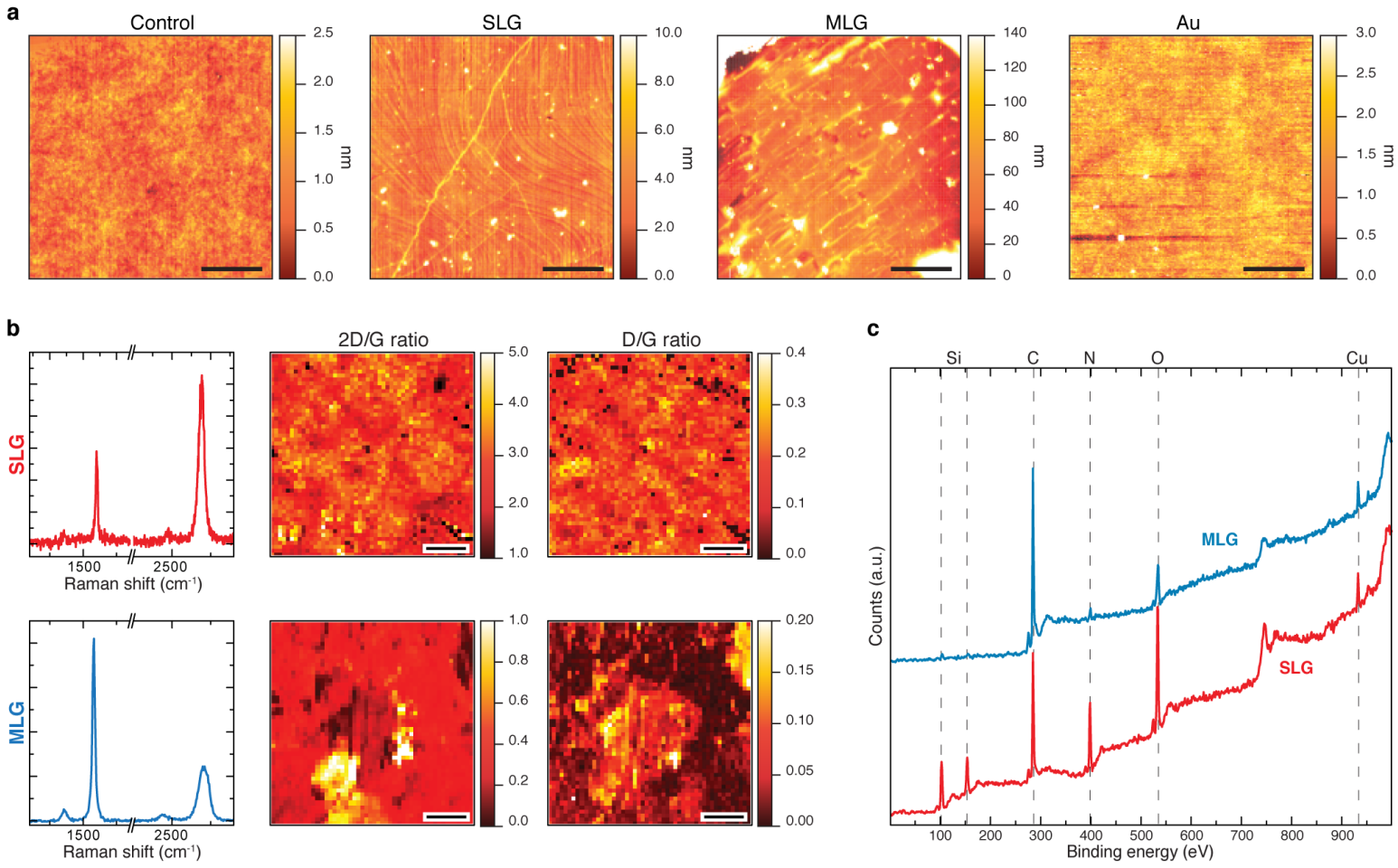
a
Control
SLG
MLG
Au
nm
b
SLG
MLG
2D/G ratio
D/G ratio
Raman shift (cm-1)
1500
2500
c
Si
C
N
O
Cu
MLG
SLG
Counts (a.u.)
Binding energy (eV)

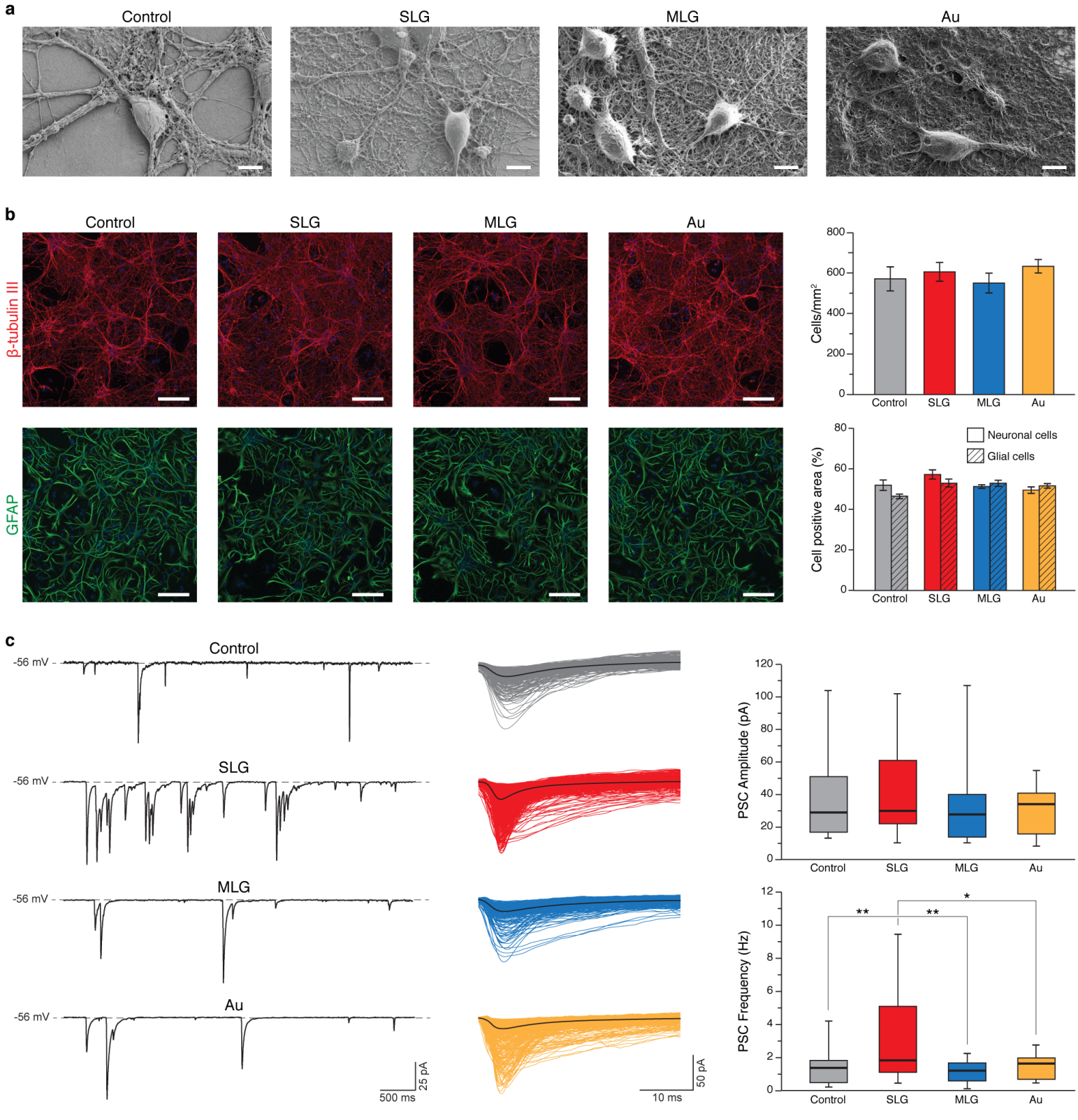
a
Control
SLG
MLG
Au
b
Control
SLG
MLG
Au
β-tubulin III
GFAP
Cells/mm²
800
600
400
200
0
Control
SLG
MLG
Au
Cell positive area (%)
80
60
40
20
0
Neuronal cells
Glial cells
c
Control
-56 mV
SLG
-56 mV
MLG
-56 mV
Au
-56 mV
25 pA
500 ms
50 pA
10 ms
PSC Amplitude (pA)
120
100
80
60
40
20
0
PSC Frequency (Hz)
12
10
8
6
4
2
0
**
**
*

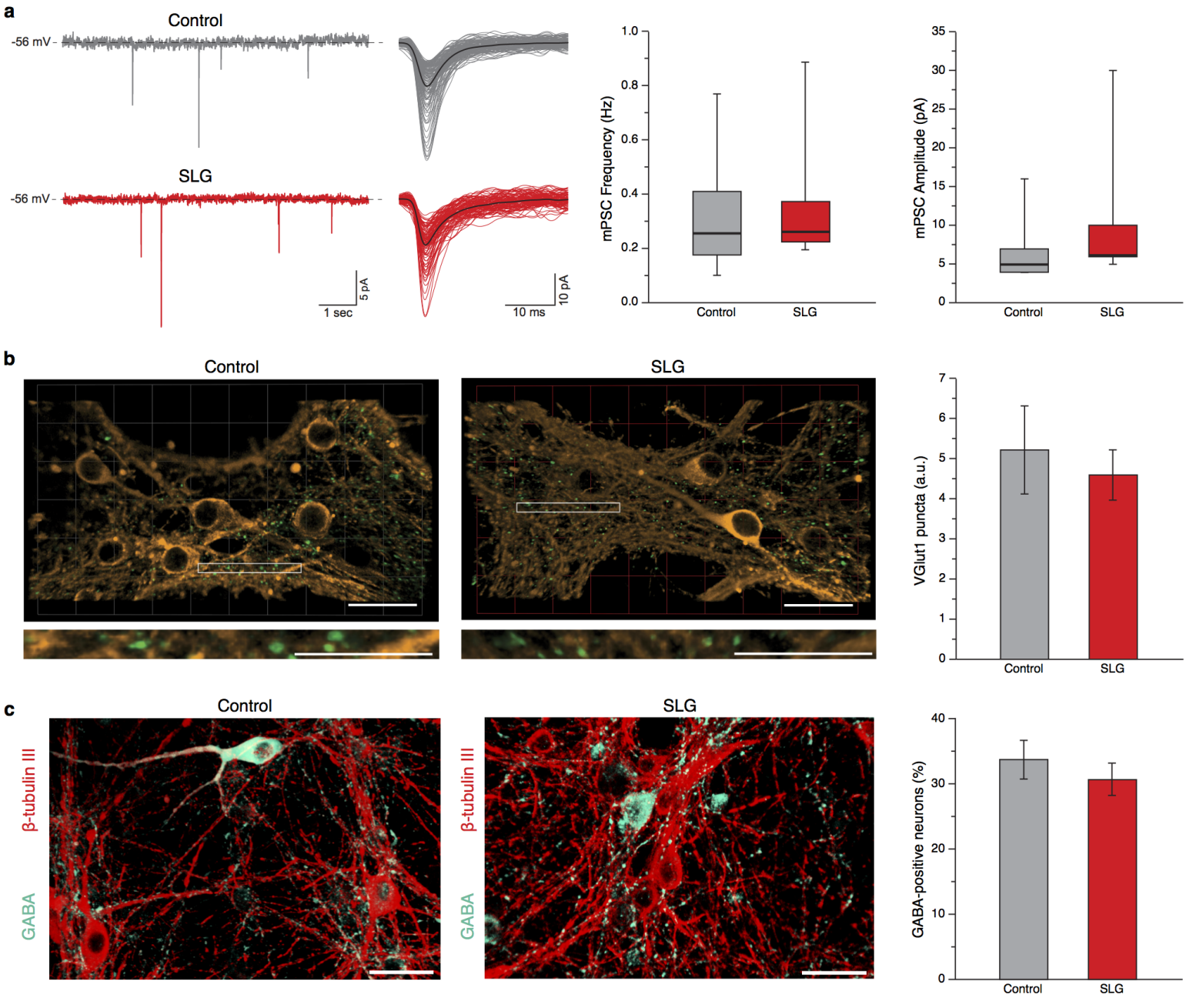
a
Control
-56 mV
SLG
-56 mV
5 pA
1 sec
10 pA
10 ms
mPSC Frequency (Hz)
1.0
0.8
0.6
0.4
0.2
0.0
Control
SLG
mPSC Amplitude (pA)
35
30
25
20
15
10
5
0
Control
SLG
b
Control
SLG
VGlut1 puncta (a.u.)
7
6
5
4
3
2
1
0
Control
SLG
c
Control
SLG
β-tubulin III
GABA
β-tubulin III
GABA
GABA-positive neurons (%)
40
30
20
10
0
Control
SLG

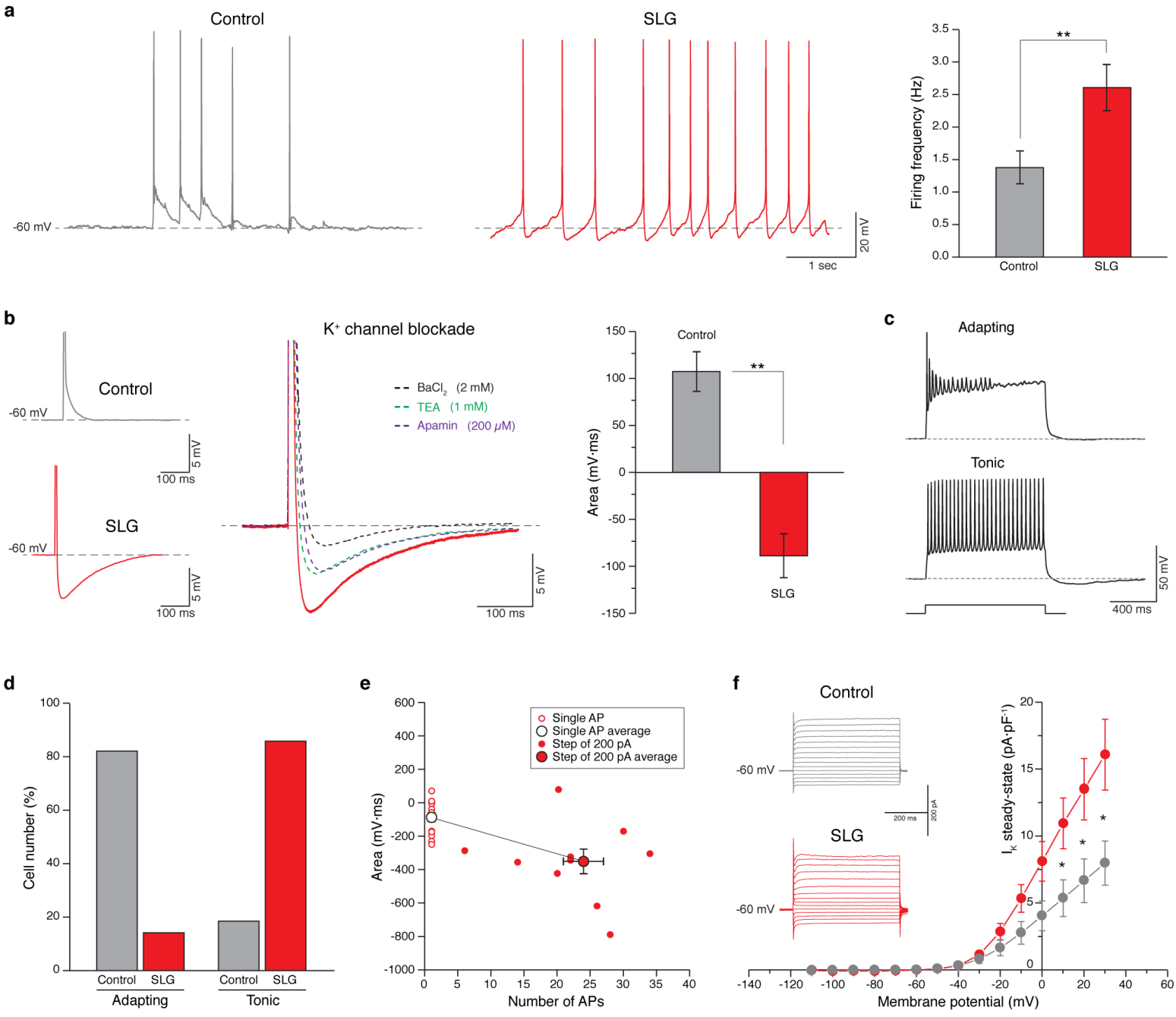
a
Control
SLG
-60 mV
20 mV
1 sec
Firing frequency (Hz)
**
Control
SLG
b
Control
-60 mV
5 mV
100 ms
SLG
K+ channel blockade
BaCl2 (2 mM)
TEA (1 mM)
Apamin (200 μM)
Area (mV·ms)
c
Adapting
Tonic
50 mV
400 ms
d
Cell number (%)
Control
SLG
Adapting
Tonic
e
Single AP
Single AP average
Step of 200 pA
Step of 200 pA average
Area (mV·ms)
Number of APs
f
Control
SLG
200 ms
200 pA
I_K steady-state (pA·pF⁻¹)
Membrane potential (mV)

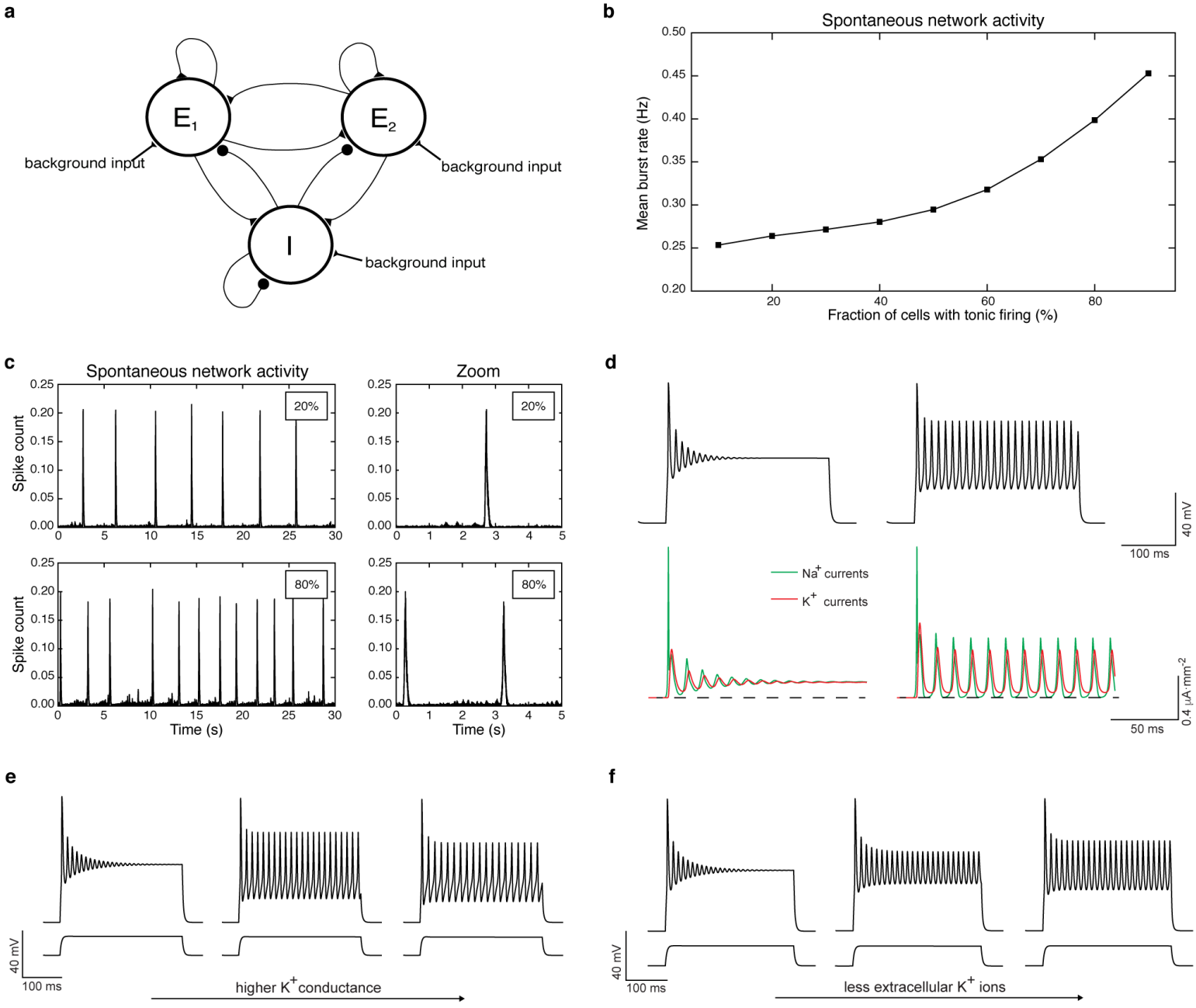
a
E1
E2
I
background input
background input
background input
b
Spontaneous network activity
Mean burst rate (Hz)
Fraction of cells with tonic firing (%)
c
Spontaneous network activity
Zoom
Spike count
20%
80%
Time (s)
d
Na+ currents
K+ currents
40 mV
100 ms
50 ms
0.4 µA·mm-2
e
40 mV
100 ms
higher K+ conductance
f
40 mV
100 ms
less extracellular K+ ions

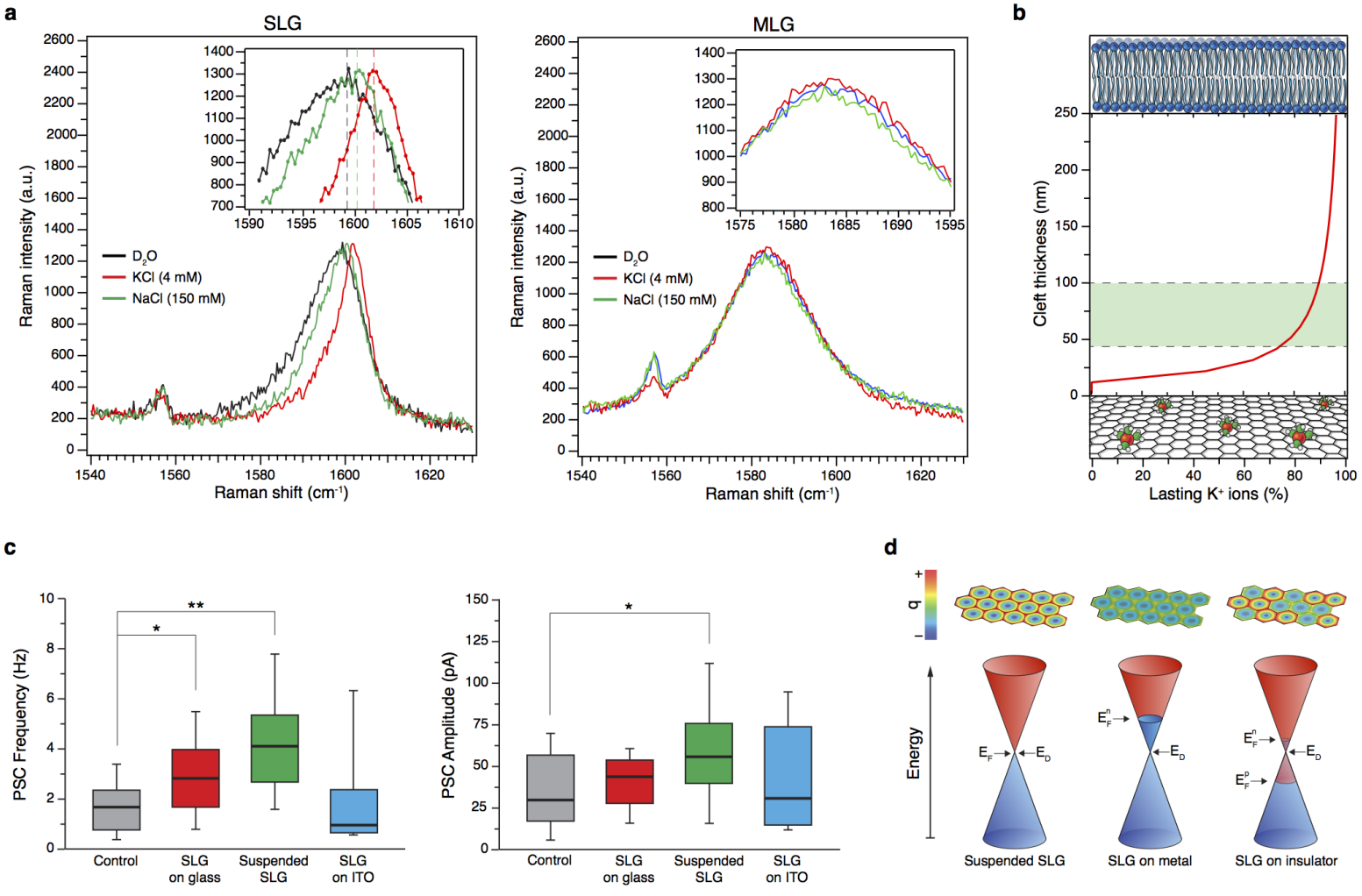
a
SLG
MLG
Raman intensity (a.u.)
Raman shift (cm⁻¹)
D2O
KCl (4 mM)
NaCl (150 mM)
b
Cleft thickness (nm)
Lasting K⁺ ions (%)
c
PSC Frequency (Hz)
PSC Amplitude (pA)
Control
SLG on glass
Suspended SLG
SLG on ITO
d
q
Energy
Suspended SLG
SLG on metal
SLG on insulator